AFRL-AFOSR-VA-TR-2024-0108

High-index dielectric metasurfaces for enhanced magneto-optics

Capasso, Federico
PRESIDENT AND FELLOWS OF HARVARD COLLEGE
1033 MASSACHUSETTS AVE STE 3
CAMBRIDGE, MA, 02138
USA

01/18/2024
Final Technical Report

Air Force Research Laboratory
Air Force Office of Scientific Research
Arlington, Virginia 22203
Air Force Materiel Command

REPORT DOCUMENTATION PAGE

PLEASE DO NOT RETURN YOUR FORM TO THE ABOVE ORGANIZATION.

1. REPORT DATE	2. REPORT TYPE	3. DATES COVERED	
20240118	Final	START DATE 20190915	END DATE 20230914

4. TITLE AND SUBTITLE
High-index dielectric metasurfaces for enhanced magneto-optics

5a. CONTRACT NUMBER	5b. GRANT NUMBER	5c. PROGRAM ELEMENT NUMBER
	FA9550-19-1-0352	61102F
5d. PROJECT NUMBER	**5e. TASK NUMBER**	**5f. WORK UNIT NUMBER**

6. AUTHOR(S)
Federico Capasso

7. PERFORMING ORGANIZATION NAME(S) AND ADDRESS(ES)
PRESIDENT AND FELLOWS OF HARVARD COLLEGE
1033 MASSACHUSETTS AVE STE 3
CAMBRIDGE, MA 02138
USA

8. PERFORMING ORGANIZATION REPORT NUMBER

9. SPONSORING/MONITORING AGENCY NAME(S) AND ADDRESS(ES)	10. SPONSOR/MONITOR'S ACRONYM(S)	11. SPONSOR/MONITOR'S REPORT NUMBER(S)
Air Force Office of Scientific Research 875 N. Randolph St. Room 3112 Arlington, VA 22203	AFRL/AFOSR RTB1	AFRL-AFOSR-VA-TR-2024-0108

12. DISTRIBUTION/AVAILABILITY STATEMENT
A Distribution Unlimited: PB Public Release

13. SUPPLEMENTARY NOTES

14. ABSTRACT
The magneto-optical effect lies at the heart of many non-reciprocal devices such as isolators and circulators. Since it is a very weak effect that linearly scales with the size of the magneto-optic material, the resulting devices tend to be bulky. This makes free-space applications cumbersome, but moreover precludes the realization of highly integrated, field-deployable devices. The goal of this work is to design, fabricate and test resonant metasurfaces to enhance the magneto-optic effect in low-loss dielectrics. Furthermore, we endeavor to employ the insight from this proof-of-concept research to experimentally realize waveguide-based non-reciprocal devices such as on-chip optical isolators. Various approaches were utilized. First the exploration of promising but little studied magneto-optical materials such as Europium Sulfide (EuS) with a large Verdet constant. In parallel resonant effects that have the potential advantage of enhancing the Faraday rotation with greatly reduced bulk were studied. This includes on-chip magneto-optic devices based on metasurfaces that enhance polarization rotation. Here the new working principle is based on guided wave resonance to enhance the Faraday rotation. This resonance occurs in suitably designed EuS metasurface 2D photonic crystals. The third approach focused on exploring new nonreciprocal design concepts. The investigation concentrated on structures dubbed cascaded mode converters that enabled the demonstration of new resonators, with performance radically different from Fabry-Perot devices.

15. SUBJECT TERMS

16. SECURITY CLASSIFICATION OF:			17. LIMITATION OF ABSTRACT	18. NUMBER OF PAGES
a. REPORT	b. ABSTRACT	c. THIS PAGE		
U	U	U	UU	26

19a. NAME OF RESPONSIBLE PERSON	19b. PHONE NUMBER *(Include area code)*
WOODDY MILLER	000-0000

Standard Form 298 (Rev.5/2020)
Prescribed by ANSI Std. Z39.18

Final Performance Report
AFOSR Grant Number: FA9550-19-1-0352
High-index dielectric metasurfaces for enhanced magneto-optics
Reporting Period: 09/15/2019– 09/14/2023
Program Manager: Lt. Wooddy Miller

PI: Prof. Federico Capasso
John A. Paulson School of Engineering and
Applied Sciences, Harvard University
Pierce Hall 205A
29 Oxford St.
Cambridge MA 02138
Tel. 617-3847611
Email: capasso@seas.harvard.edu

1. Goals

The magneto-optical effect lies at the heart of many non-reciprocal devices such as isolators and circulators. Since it is a very weak effect that linearly scales with the size of the magneto-optic material, the resulting devices tend to be bulky. This makes free-space applications cumbersome, but moreover precludes the realization of highly integrated, field-deployable devices. The goal of this work is to design, fabricate and test resonant metasurfaces to enhance the magneto-optic effect in low-loss dielectrics. Furthermore, we endeavor to employ the insight from this proof-of-concept research to experimentally realize waveguide-based non-reciprocal devices such as on-chip optical isolators. Various approaches were utilized. First the exploration of promising but little studied magneto-optical materials such as Europium Sulfide (EuS) with a potentially large Verdet constant. In parallel resonant effects that have the potential advantage of enhancing the Faraday rotation with greatly reduced bulk were studied. This includes on-chip magneto-optic devices based on metasurfaces that enhance polarization rotation. Here the new working principle is based on guided wave resonance to enhance the Faraday rotation. This resonance occurs in suitably designed EuS metasurface 2D photonic crystals. The third approach focused on exploring new nonreciprocal design concepts. The investigation concentrated on structures dubbed cascaded mode converters that enabled the demonstration of new resonators, with performance radically different from Fabry-Perot devices

2. Accomplishments

- Investigation of properties (optical, X-ray diffraction) of Europium Sulfide (EuS) films for novel magneto-optical devices
- Guide-wave resonance metasurface magneto-optical device: design, simulations, fabrication, and measurements
- New nonreciprocal devices: cascaded mode resonators. Design, simulations, fabrication, and measurements

3. Metasurface based magneto-optical devices

3.1 - The magneto-optic effect

The most important MO effects (Faraday and Kerr effects) occur due to the splitting of energy levels of a MO material in an external magnetic field [*AK Zvezdin, VA Kotov, Modern magnetooptics and magnetooptical materials*, Taylor&Francis, 1997]. The ground and excited states of such systems become nondegenerate for light carrying distinct spin angular momenta. The MO material exhibits different refractive indices for left and right circularly polarized light:

$$n_{\pm}(\omega) \approx n(\omega) \pm \frac{dn}{d\omega}\frac{eH}{2mc} \tag{1}$$

where $n(\omega)$ is the refractive index in the absence of the field H, n_+ and n_- are the refractive indices of left and right circularly polarized light, respectively, e and m are the electron charge and mass and c is the speed of light in vacuum. Linearly polarized light propagating in this medium along the z-axis has the form

$$E = \frac{1}{2}E_o e^{-i(wt-2\pi nz/\lambda)}[\hat{x}\cos\theta + \hat{y}\sin\theta] \tag{2}$$

where $\hat{x}$ and $\hat{y}$ are the unit vectors along the x- and y-axis.
When light travels a distance L inside the MO crystal, the polarization of light rotates by an angle:

$$\theta = \frac{k(n_+ - n_-)L}{2}, \tag{3}$$

where k is the wavevector of the incident light, L is the thickness of the MO medium and n_+, n_- are the refractive indices along the x and y axis, respectively.
This expression can be rewritten using the Verdet constant V, which determines the angle of rotation per unit length and per unit field strength B:

$$\theta = VBL. \tag{4}$$

The MO effect radically differs from optical activity associated with chiral media. When light travels multiple times back and forth through a MO material, the polarization rotation angle accumulates. This effect occurs due to broken time-reversal symmetry imposed by the magnetic field. Thus, the device is inherently nonreciprocal. Hence, large polarization rotation angles can be achieved by cycling through the same volume multiple times.

The effect of polarization rotation has been used in a wide variety of practical applications. An optical isolator (diode) is one of the basic devices that exploits this effect in MO materials, and an important building block. The schematic of a Faraday isolator is shown in Fig. 1. This device allows light to propagate only in one direction while blocking it in the opposite direction. It consists of a MO material placed in between two polarizers. The main axes of these polarizers are rotated by 45 degrees with respect to each other. Typically, a permanent magnet is placed around the MO material.

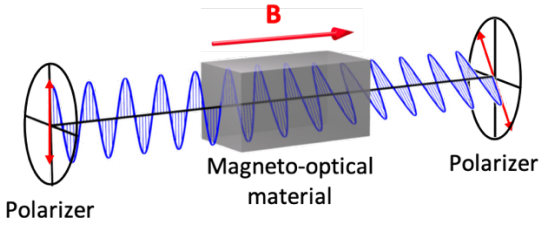

Fig. 1 - Schematics of a conventional optical isolator. The polarization of light is rotated by 45 degrees when light propagates through the MO material. A pair of polarizers ensures that light can be transmitted only in one direction.

Light traveling in the forward direction becomes linearly polarized by the input polarizer. The MO material rotates the polarization of light by 45 degrees. A second polarizer oriented at 45 degrees lets the rotated light pass. However, when light travels in the opposite direction, it becomes polarized at 45 degrees by the second polarizer and the MO material rotates it by an additional 45 degrees. The resulting polarization is perpendicular to the axis of the input polarizer, and therefore backward propagating light is blocked.
MO devices that exploit the Faraday roation are typically long and bulky. We searched therefore for physical mechansims that would allow us to reudce length and overall size and for MO materials with large Verdet constant.

For MO material we chose Europium Sulphide (EuS). This material posseses a number of advantages: a high Verdet constant in the visible spectral range (superior to TGG), low absorption and it can be deposited via thermal evaporation. The latter is of particular importance for the fabrication aspect of this work, as described below. The material, desposited by e-beam evaporation, is grown by Prof. Jagadeesh Moodera (MIT), as part of a collaboration with our group

3.3 Characterization of Europium sulfide: ellipsometry, x-ray diffraction and Verdet constant measurements

A spectroscopic ellipsometer (J. A. Woollam V-VASE32) was used to measure the refractive index of EuS in the visible spectral range. We fabricated two samples (Fig. 2) for these measurements. The first sample consists of a 20 nm thick Alumina layer deposited on the 0.5 mm thick Si substrate. The second sample consist of three layers where 50 nm thick EuS is sandwiched in between two 20 nm layers of Al_2O_3. These two layers are deposited to protect EuS from oxidation and to ensure good adhesion to the substrate. Deposition of Al_2O_3 on Si was performed simultaneously for both samples. Refractive index of Al_2O_3 is obtained from the first sample, and fed into the model that is used for sample with EuS layer. Real and imaginary parts of the refractive index measured for EuS are plotted in Fig. 4.

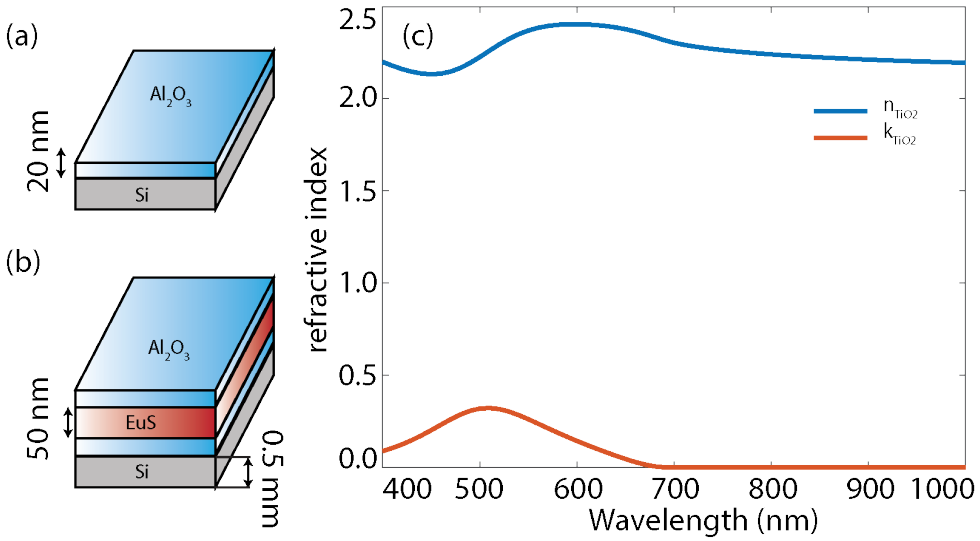

Fig. 2 - Refractive index measurement of EuS using ellipsometry. (a): Sample structure fabricated for measurement of Al_2O_3 layer refractive index. (b): Sample structure used for EuS refractive index measurements. 20 nm thick Al_2O_3 layers are added to ensure adhesion of EuS and prevent it from oxidation. (c): Real and imaginary part of refractive index for EuS extracted from ellipsometry measurements.

To confirm the purity of the material we performed x-ray difraction (XRD) analysys of the EuS powder used in the fabrication. The XRD spectrum is shown in Fig. 3. We found that peaks of the measured spectrum are in excellent correspondance to EuS XRD pattern available in crystalographyc databases.

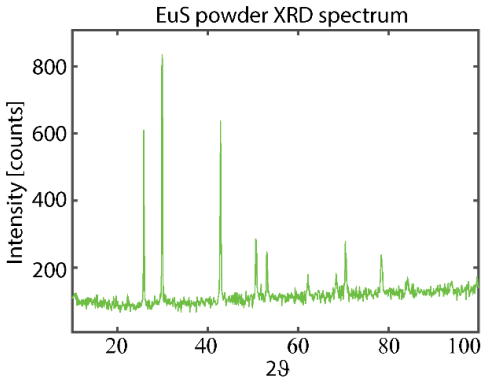

Fig. 3 - XRD measurement of EuS powder. Peaks show excellent agreement with the crystallographic database and confirm the purity of the used material.

To determine the Verdet constant of the EuS we built a custom setup for Faraday rotation measurements. We fabricated samples with 1 μm thick EuS on 0.5 mm thick quartz glass. Considering that glass is 2 orders of magnitude thicker than EuS, its polarization rotation action on light should be taken into accout.

As a first step we measured Verdet constant of quartz glass without EuS layer. Measured data are plotted in Fig. 4. The Verdet constant of glass is extracted from this measurement and is V_{Glass}=1.58±0.02 rad/mT. ($V_{pyrex} = 3\ \frac{rad}{mT}$ and $V_{SF57} = 20\ \frac{rad}{mT}$ at λ=632 nm). We measured the polarization rotation of quartz glass with EuS layer. The results of the measurements are shown in Fig. 6. The rotation caused by EuS layer can be calculated as

$$\theta_{EuS} = \theta_{glass} - \theta_{EuS\ on\ glass}. \qquad (5)$$

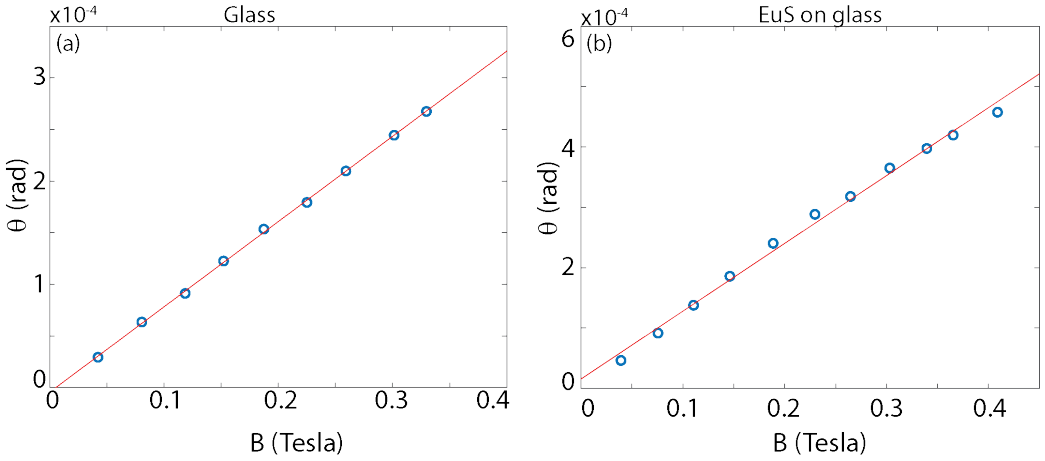

Fig. 6 - Verdet constant measurements. (a) Polarization rotation angle as a function of applied magnetic field for glass sample. (b) Polarization rotation angle as a function of applied magnetic field for glass sample with 1 μm thick EuS layer. Red lines in both images are linear fits to the data.

The angle of rotation for EuS on glass is subtracted from the angle of rotation for glass substarte, because the Verdet constant of EuS has negative sign in this wavelength region. Once the angle of rotation is known we obatin the Verdet constant of EuS to be $V_{EuS} = 2000 \pm 17\ \frac{rad}{mT}$. at room temperature [M.L. Meretska, et al. *Applied Physics Letters*, 120, 25 (2022)].

4. Guide-wave resonance metasurface magneto-optical device

4.1 – Metasurface-based free-space Faraday isolator

Some dielectric materials, such as Terbium Gallium Garnet (TGG), naturally possess a relatively high Verdet constant. TGG is commercially used in an optical isolator in the visible spectral range. Despite its relatively high Verdet constant, the resulting device dimensions are still in the order of tens of centimeters because MO effects are intrinsically weak. We aim to design metasurfaces using resonant structures based on EuS to allow for a more compact device at the micrometer scale.

The principle of miniaturizing the device based on EuS-based resonant metasurfaces is to trap the light inside the metasurface and accumulate the polarization rotation of the light through travelling back and forth multiple times. Note that the polarization rotation will keep accumulating and not be cancelled out during one back-and-forth cycle because of the non-reciprocal nature of MO effects [A K Zvezdin & V A Kotov,*Modern magnetooptics and magnetooptical materials*, 1997]. Therefore, with this metasurface, incident light experiences enhanced Faraday rotation at the resonance frequency compared to when it passes through a uniform film of the same material. However, resonances are usually accompanied by strong transmission and reflection changes so careful design is necessary to obtain a high transmittance at the resonance frequency. Additionally, a high quality factor (Q factor) is preferred because it indicates stronger light trapping within the metasurface, leading to a longer back-and-forth travel distance of light, and consequently, a larger Faraday rotation. In the next section, we will be studying a metasurface that is based on a EuS lattice (Fig. 7 (a)), along with the guided mode resonances that occur within it.

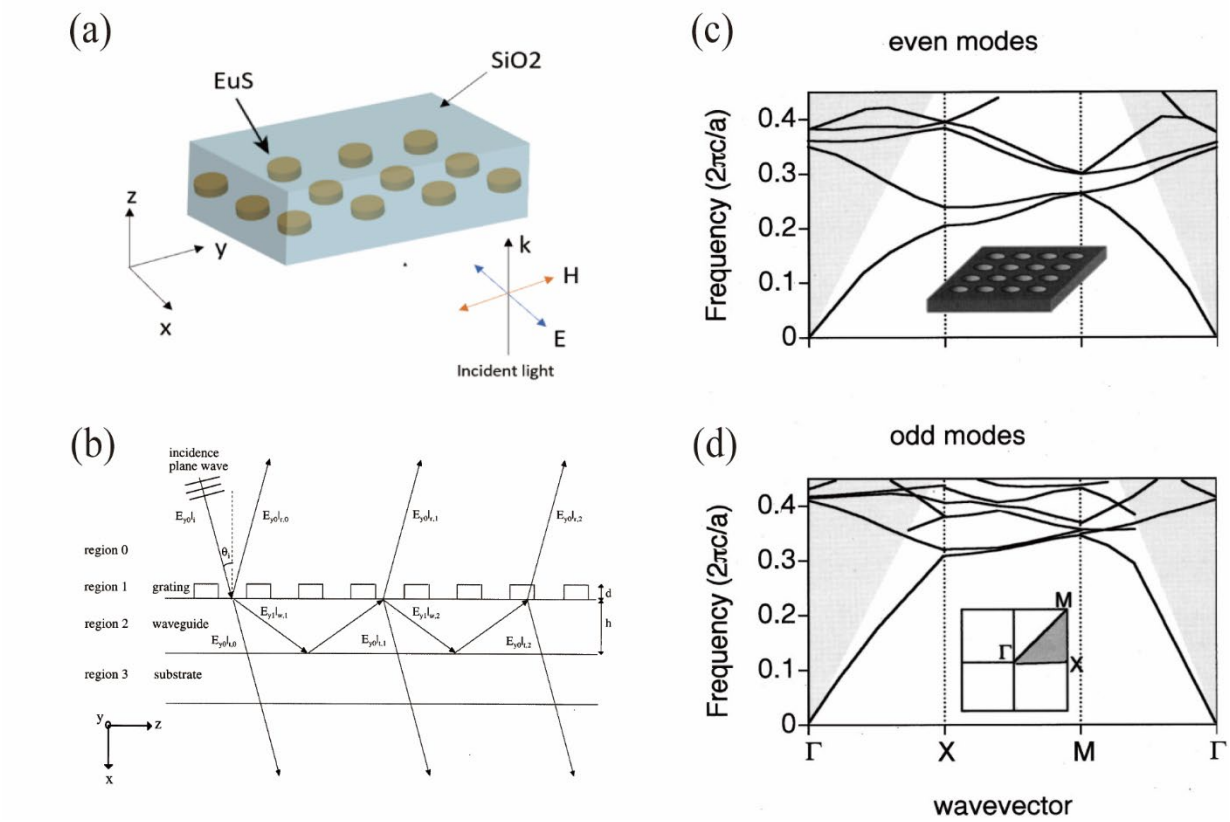

Fig. 7 Guided mode resonances (a) Schematics of the simulated structure of a EuS metasurface embedded in SiO2. (b) Principle of the guided mode resonance in a grating-waveguide structure with the ray optics picture. As a result of the interference between the partial waves reflected by the resonant grating the incident wave experiences high reflectivity at a certain wavelength and orientation angle. (c) Even and (d) odd mode band structure diagrams in a photonic crystal slab. The structure is shown in the inset of (c) and consists of a square lattice of air holes with the lattice constant **a** in a high-index dielectric slab. Even and odd modes are separated based on the field profile symmetry with respect to the mirror plane parallel to the slab. The gray region is the continuum of radiation modes above the light line. Solid lines outside the gray region are guided modes. Solid lines within the gray region are guided mode resonances.

4. 2 – Guided mode resonances in the EuS metasurface

As mentioned above, the designed metasurface is a 2-dimensional array composed of EuS pillars embedded in SiO2 matrix, as shown in Fig. 7 (a). This structure is also known as a photonic crystal (PhC) slab, which consists of a thin layer of material that has a periodic pattern of high and low refractive index regions. PhC slabs are well-known for supporting guided modes and guided mode resonances, which allow for various applications such as optical filters, waveguides, and sensors. The principle of guided mode resonances is shown in Fig. 7 (b) [A. Sharon, D. Rosenblatt, and A. A. Friesem, *JOSA A*, 14, 2985 (1997)]. The structure shown consists of a diffraction grating and a waveguide slab. The incident light is divided into three parts on the grating: directly reflected light, directly transmitted light, and diffracted light. Some of the diffraction orders match the waveguide modes of the structure, making the diffracted light confined in the waveguide. The confined light can be coupled out of the structure when it hits the grating again during each cycle. Therefore, the directly reflected/transmitted light and the light leaked from waveguide modes contribute to sharp resonant peaks/dips in the reflection/transmission spectrum, which is an important feature of guided mode resonances. The reflection and transmission of guided mode resonances can be modelled by the Fano resonance [U. Fano *Physical Review*, 124, 1866, (1961)], which describes the resonance effects where the transmission/reflection property is determined by the interference between direct and indirect light pathways. In the case of guided mode resonances, the transmitted amplitude *t* and the reflected amplitude *r* can be expressed as follows [Shanhui Fan and J. D. Joannopoulos *Physical Review B*, 65, 235112, (2002)]:

$$t = t_d + f\frac{\gamma}{i(\omega-\omega_0)+\gamma} \ , \tag{6}$$

$$r = r_d \pm f\frac{\gamma}{i(\omega-\omega_0)+\gamma} \ . \tag{7}$$

Here t_d and r_d are the direct transmission and reflection coefficients, ω_0 and γ are the center frequencies and widths of the Lorentzian from the resonance, and the factor f is the complex amplitude of the resonant mode. The plus and minus sign in Eq. (7) is determined by the field symmetry of the resonant mode. This model can give a good fitting to the line shapes of guided mode resonances.

Although a PhC slab lacks a distinct waveguide, its lattice structure can function as both a diffraction grating and a waveguide, so the same theory can be applied to PhC slabs. The waveguide modes in a PhC slab can be simply called guided modes, which are usually visualized by the band structure diagrams. An example is shown in Fig. 7(c)(d) [Shanhui Fan and J. D. Joannopoulos *Physical Review B*, 65, 235112, (2002)]. The two band structure diagrams describe the relationship between the frequency ω and the transverse wavevector component k_T of guided modes in a PhC slab consisting of a square lattice of air holes in a high-index dielectric matrix. The letters on the horizontal axis represent the three high-symmetry points in the Brillouin zone, as shown in the inset of Fig. 7 (d). This axis describes the wavevector path from Γ to X, to M, and back to Γ in the Brillouin zone. Additionally the are separated into guided modes into even and odd modes based on the field profile symmetry with respect to the mirror plane parallel to the slab. The even and odd modes are also known as TE (transverse electric) and TM (transverse magnetic) modes, respectively, based on the mirror reflection symmetry property of the electric and magnetic fields. It is also worth noting that the light line, which is defined as the boundary between the white region and the gray region, represent the ω-k_T relationship when the square of the *z* component of the wavevector k_z^2 equals to zero. Below the light line, k_z is an imaginary number since $k_z^2 < 0$, which indicates the field is evanescent in the *z* direction and the modes in the white region are protected inside the PhC slab without coupling out, while above the light line, k_z is an real number since $k_z^2 > 0$, which indicates the field is propagating in the *z* direction and the modes in the gray region are radiating out of the PhC slab. Therefore, the modes in the gray region show where guided mode resonances occur. In simulations or experiments, to demonstrate a guided mode resonance that is found from the band structure, one can set the frequency of the incident light as the frequency of the target mode and tune the incident angle of the light to make the incident k_T equal to the k_T of the target mode.

4.3 Parameter study of the EuS metasurface

Three geometrical parameters need to be determined in the parameter study: the lattice period a, the pillar radius R, and the pillar thickness L (see the inset of Fig. 8). Considering both the Verdet constant and absorption coefficient spectra of EuS [M.L. Meretska, et al. *Applied Physics Letters*, 120, 25 (2022)], we decided to do the study for the wavelength range between 700-800 nm, where EuS has both a relatively high Verdet constant and a relatively low absorption coefficient. For simplicity, normal incidence is used, and no absorption is considered in this simulation. Based on the guided mode resonance theory, we did a parameter sweep simulation with a reasonable parameter range and found two guided mode resonance dips in the transmission spectrum. When $a = 500\ nm, R = 230\ nm, L = 140\ nm$, the transmission spectrum is shown in Fig. 2. The left resonance dip with a sharp line shape indicates a high-Q resonance, while the right resonance dip with a broader linewidth indicates a relatively low-Q resonance. Both resonances exhibit residual transmittance.

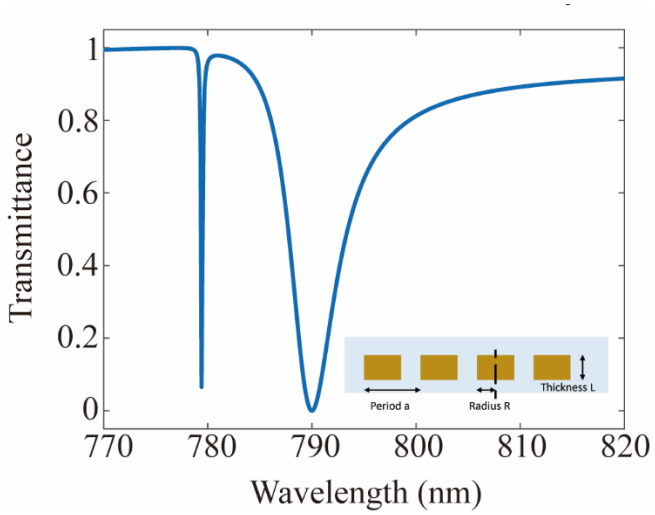

Fig. 8 – **Transmittance spectrum of the designed geometry in normal incidence**. The three geometrical parameters period a=500 nm, pillar radius R=230 nm, and pillar thickness L=140 nm. No material absorption is assumed. A high-Q resonance and a low-Q resonance are found in the wavelength range between 700-800 nm. The inset shows a side view of the structure and the three geometrical parameters.

To further characterize these two resonances, we conducted two additional parameter sweep simulations. First, we examined how the spectral positions of the high-Q and low-Q resonances vary with changes in the lattice periods in the x and y directions (a_x and a_y), while maintaining other parameters constant. The findings are presented in Fig. 3. In Fig. 9 (a), we vary a_x while preserving $a_y = 500\ nm$. The low-Q resonance's spectral position, marked by the white dashed line, remains almost constant. However, the high-Q resonance's spectral position, marked by the red dashed line, significantly depends on a_x. As a contrast, in Fig. 0 (b), we observe that the low-Q resonance's spectral position shifts with changes in a_y, but the high-Q resonance's position remains largely unaffected. These results show that the high-Q and low-Q resonances are exclusively related to the x and y directions, respectively, suggesting the directionality of their underlying guided modes.

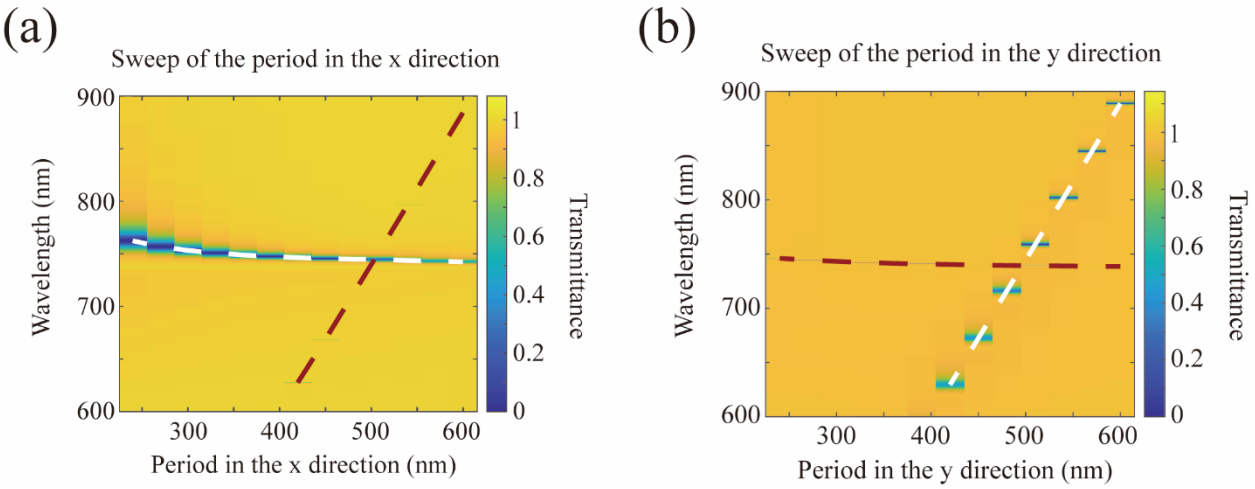

Fig 9 Transmittance spectra map for varying lattice periodicity in the x and y directions. (a) The change of the period in the x direction causes the high-Q resonance to spectrally shift. (b) The change of the period in the y direction causes the low-Q resonance to spectrally shift. The dashed lines in (a) and (b) trace the positions of the two resonances, where the low-Q resonance is outlined with the white dashed line and the high-Q resonance is traced with the red dashed line.

The second simulation is to examine the responses of the resonances to small changes in the incidence angle. In this simulation, all the geometrical parameters are kept constant, and the incident plane is fixed as the *x*-*z* plane, which means that the incident transverse wavevector k_T is along the *x* direction. We set the incident polarization as s-polarization (polarization perpendicular to the incidence plane) or p-polarization (polarization parallel to the incidence plane) and sampled a few small incidence angles from 0.2 to 1.2 degrees. Some results are shown in Fig. 10. In the case of normal incidence, as shown in Fig. 8, we observe one high-Q resonance and one low-Q resonance. However, when the incidence angle is non-zero, resonance splitting occurs. Specifically, for p-polarization incidence, the high-Q resonance is split into two, while the low-Q resonance at the wavelength of 755 nm is unaffected (see Fig. 10 (a)(b)). As a contrast, for s-polarization incidence, the low-Q resonance is split into two, while the high-Q resonance around the wavelength of 755 nm is almost unchanged (see Fig. 10 (c)(d)). In addition, when the incidence angle increases, the split resonances shift farther apart from each other for both polarization situations. The resonance splitting indicates that both the high-Q and low-Q resonances might correlate with doubly degenerate guided modes, and that these modes are sensitive to small-angle oblique incidence with particular polarizations.

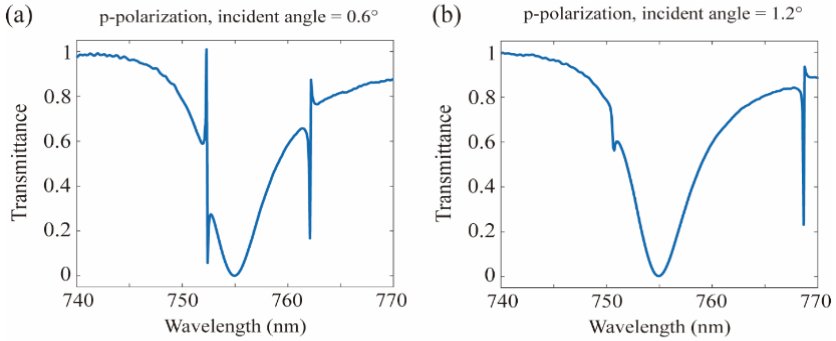

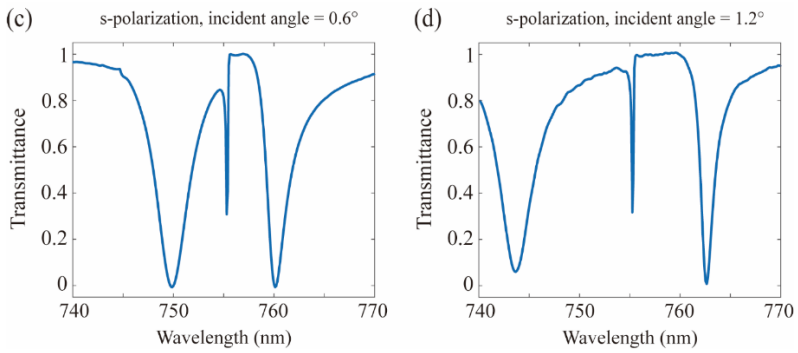

Fig. 10 – Transmittance spectra with small-angle oblique incidence and s- or p- polarization. The simulation setting for the subfigures: (a) p-polarized incident light, incidence angle= 0.6 deg; (b) p-polarized incident light, incidence angle = 1.2deg ; (c) s-polarized incident light, incidence angle= 0.6 deg; (d) s-polarized incident light, incidence angle= 1.2 deg. When incident angle is not zero, the high-Q resonance is split into two if the incident light is p-polarized, while the low-Q resonance is split into two if the incident light is s-polarized. The larger the incidence angle is, the farther the split resonances shift apart from each other.

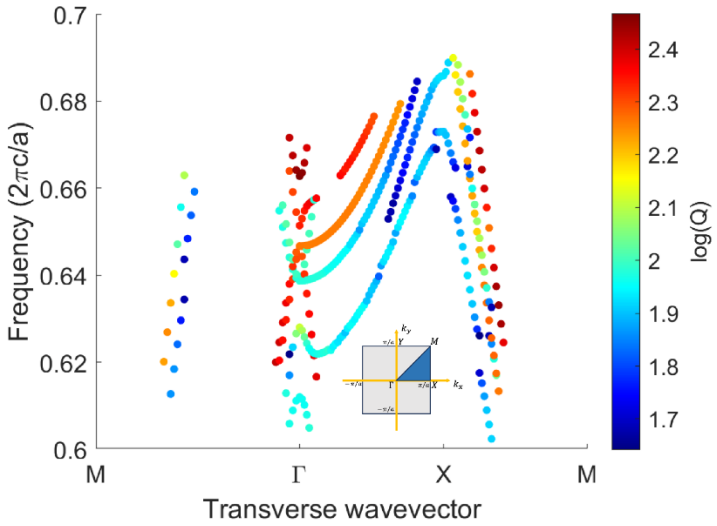

Fig. 10 Band structure of the designed metasurface in the frequency region of interest. The frequency in the y axis is normalized by the factor 2πc/a, where c is the speed of light and a is the lattice constant. The color of each sample point marks the log value of its Q factor. The inset shows the Brillouin zone of the designed structure.

4.5 – Mode analysis based on the band structure

To better understand the nature of the high-Q and low-Q resonances, we calculated the band structure of the designed device to look for the guided modes related to the two resonances. We set the geometrical parameters $a = 500\ nm, R = 230\ nm, L = 140\ nm$ (the same setting as in Fig. 8) and searched for modes around the wavelength of 785 nm. The calculated band structure diagram is shown in Fig. 10. Same as in Fig. 7 (c)(d), the horizontal -axis is the path of the transverse wavevector k_T in the Brillouin zone (see the inset of Fig. 10), and the *y*-axis is the mode frequency normalized by $2\pi c/a$. The color of each sample point marks its Q factor. Fig. 10 shows that there are many bands in this region, which makes it hard to identify the modes related to the resonances we observed. For clarity, we only keep the k_T range from Γ to X ($k_T = k_x$ in this case) and divide all the modes into TE and TM modes, as shown in Fig. 11 (a)(b). Based on the results in Fig. 11, we identify the two modes circled along the *y* axis in the TE mode and TM mode

diagrams as the guided modes related to the low-Q and high-Q resonances, respectively, for at least three reasons. First, the frequencies of the TE and TM modes match the wavelengths of the low-Q and high-Q resonances in Fig. 8. It also makes sense that the TE mode has a smaller Q factor than the TM mode as marked by the color in Fig. 11(a)(b). Second, both the circled TE and TM modes are doubly degenerate modes when $k_x = 0$, and increasing k_x breaks the degeneracy. This corresponds to the observation of resonance splitting when the incident angle is not zero. Fig. 11 (c)(d) and (e)(f) show the H_z and E_z field profiles of the doubly degenerate TE and TM modes when $k_x = 0$, respectively. We can find that the double degeneracy is generated because of the two possible polarization of the fields. To understand why the high-Q and low-Q resonances are exclusively sensitive to the p-polarized and s-polarized light, respectively, one needs to understand the relationship between the incident polarization and the excited mode type. Consider normal incident light with p-polarization in the *x*-*z* plane. When it is diffracted by the PhC slab and coupled into guided modes, the polarization has to be preserved. Specifically, since the incident light has the E field in the *x* direction and H field in the *y* direction, the diffracted light propagating in the *x* direction still has its H field in the *y* direction, resulting in a TM mode, while the diffracted light propagating in the *y* direction still has its E field in the *x* direction, resulting in a TE mode. Therefore, when p-polarized light has a non-zero incident angle in the *x*-*z* plane, it gives a non-zero k_x to TM modes, leading to the degeneracy breaking of the circled TM mode and splitting of the high-Q resonance. In contrast, when s-polarized light has the same incidence angle, it will give a non-zero k_x to TE modes, leading to the degeneracy breaking of the circled TE mode and splitting of the low-Q resonance. Third, with the discussion above, we know that TE modes are polariazed in the *y* direction while TM modes arepolarized in the *x* direction for normal incidenc. Since we observed that the spectral positions of the high-Q and low-Q resonances depend exclusively on the period in the *x* direction and *y* direction, respectively, we know that the high-Q and low-Q resonances are related to a TM mode and a TE mode, respectively. *In conclusion for the parameter study and band structure analysis, the high-Q resonance is related to a doubly degenerate TM guided mode, while the low-Q resonance is related to a doubly degenerate TE guided mode.*

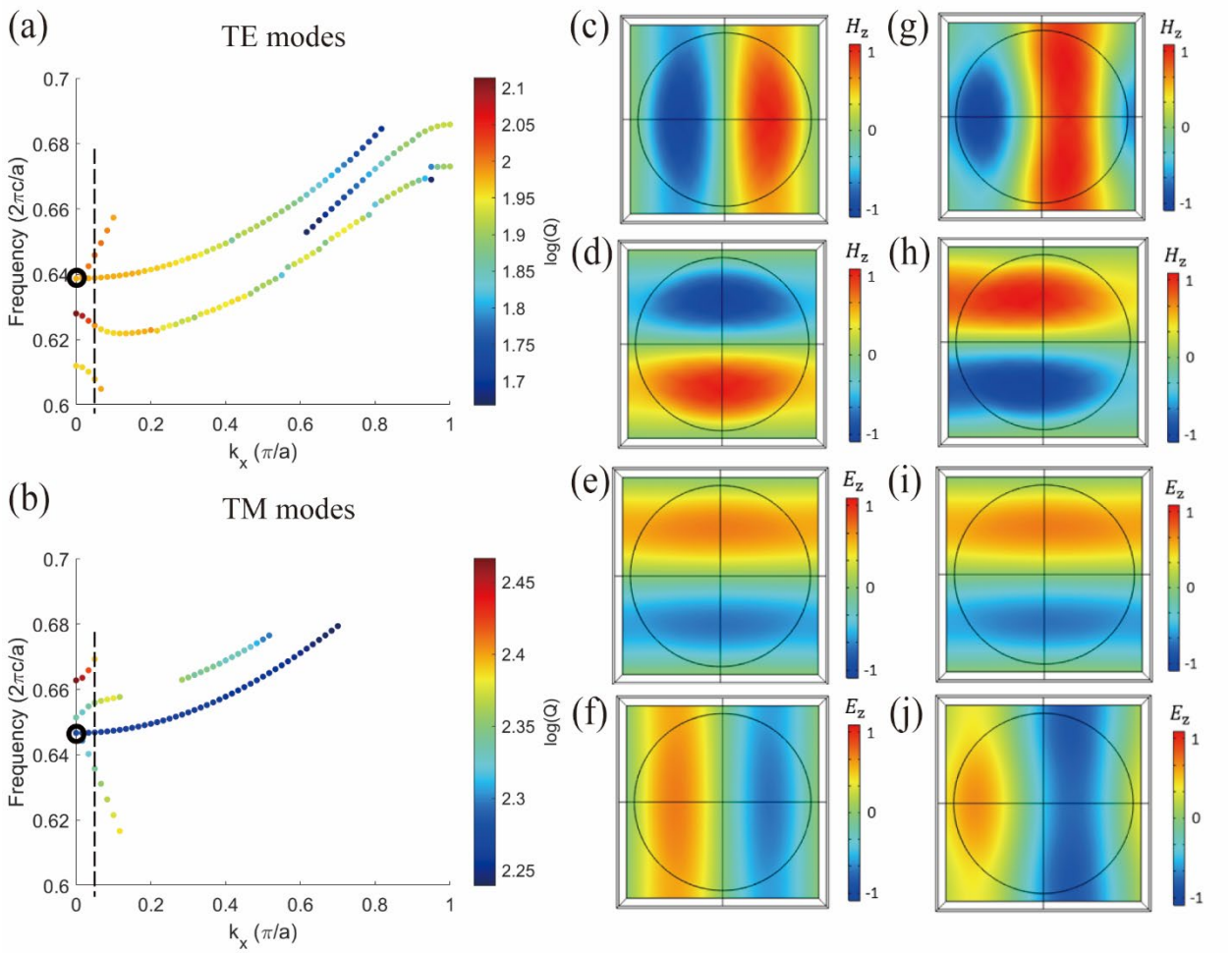

Fig. 11 – Band structure for TE (a) and TM (b) modes with the transverse wavevector from Γ to X (i.e. k_x from 0 to π/a, where a is the lattice constant) and 8 field profiles in the x-y plane. Specifically, (c) and (d) are two H_z field profiles for the doubly degenerate mode circled on the y axis in (a); (e) and (f) are two E_z field profiles for the doubly degenerate mode circled on the y axis in (b); (g) and (h) are the evolved field profiles from (c) and (d) when normalized $k_x = 0.05$, as indicated by the dashed line in (a); (i) and (j) are the evolved field profiles from (e) and (f) when normalized $k_x = 0.05$, as indicated by the dashed line in (b). These results reveal that the low-Q and high-Q resonances correspond to the doubly degenerate modes circled in (a) and (b), respectively.

4..6 – Design of a high-performance metasurface-based Faraday rotator

The resonances discussed above have the ability to produce large Faraday rotation, but show very low transmittance, as shown in Fig. 8,9,10. The reflectivity is correspondingly high but for a practical device one wourl want to achieve high transmission. We have shown that by overlapping the spectral positions of the TE and TM guided mode resonances to generate a four-fold degenerate state, high transmittance can be achieved. As shown in Fig. 12(a), we sweep the pillar radius R while keeping $a = 500\,nm$, $L = 140\,nm$, and the resonance overlapping condition is found when $R = 165\,nm$, marked by the left dashed line. Fig. 12 (b) shows the transmittance spectrum plot for this pillar radius. A near-100% transmission is achieved at the wavelength of around 755 nm, where the two resonances overlap. Note that this simulation was performed without accounting for material absorption, as it allows for precise identification of the resonances.

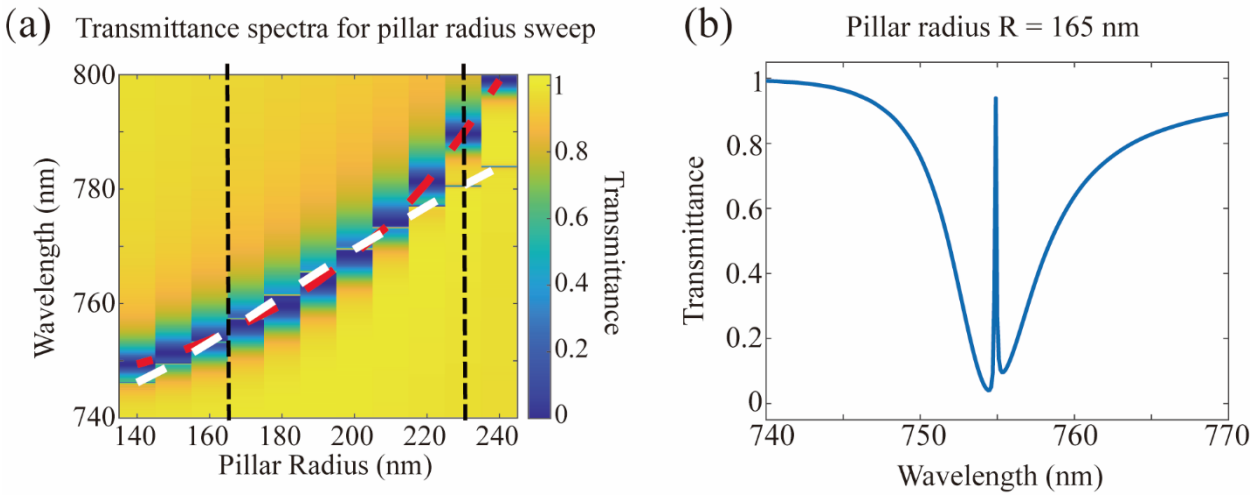

Fig, 12 – The transmittance spectra for the high-performance design. (a) The transmittance spectra map for different EuS pillar radii with the fixed parameters of the lattice constant a = 500 nm and the pillar thickness L = 140 nm. The dashed red and white lines trace the positions of the TE guided mode resonance (low-Q) and TM guided mode resonance (high-Q), respectively. (b) The transmittance spectrum when the two resonances spectrally overlap, corresponding to the left dashed line in (a). The transmittance at the resonance overlap is near 100%. The right dashed line in (a) corresponds to the spectrum in Fig. 2.

To evaluate the enhancement of the Faraday effect in this EuS metasurface, we performed simulations of the Faraday rotation angle for the two pillar radii that correspond to the overlapping and spectrally separated resonances (see Fig. 12 (b) and Fig. 7). We observe the enhancement of the Faraday effect at the spectral positions of the TE and TM guided mode resonances in the spectrally separated resonance condition, as shown in Fig. 13 (b). This is the expected result, and it demonstrates the validity of the simulation model that we used. Furthermore, the highest absolute value of the Faraday rotation is achieved at the position of the TM guided mode resonance and is equal to ~0.05 deg.

In the overlapping resonance condition, we observe an enhancement of the Faraday effect at the position of the resonance overlap, and the Faraday rotation angle is equal to ~0.18 deg, as shown in Fig. 13 (a). We observe a 3.6 times improvement compared to the spectrally separated resonance condition. Although the enhancement of the Faraday effect is clearly visible, we need to consider the transmittance of the structure at the given wavelength. It can be done by introducing the figure of merit (FOM) that is commonly used to evaluate the performance of the Faraday effect [A. B. Khanikaev, A. V. Baryshev, A. A. Fedyanin, A. B. Granovsky, and M. Inoue *Optics Express*, 15, 6612 (2007)]:

$$FOM = \sqrt{T}|\theta|. \quad (8)$$

Here T is the transmittance, and θ is the Faraday rotation angle. We plot the FOM as a function of the wavelength for the selected pillar radii (see Fig. 13 (c)(d)). The highest FOM value for the overlapping resonance condition is ~0.17, which is 5.3 times higher than the highest FOM for the spectrally separated resonance condition. In addition, we evaluated the performance of our device against a uniform EuS layer with the same thickness. The FOM value for our design is ~ 24 times higher than a thin film, demonstrating a clear superiority of the proposed geometry.

In conclusion for this section, we simulated the EuS metasurface design and achieved high transmission, large Faraday rotation, and large FOM in the condition when the TE and TM guided mode resonances spectrally overlap. This approach is more promising and practical than the Kerker condition [M. Decker, et

al. *Advanced Optical Materials*, 3, 813, 2015], which instead utilizes the resonances in each individual meta-atom.

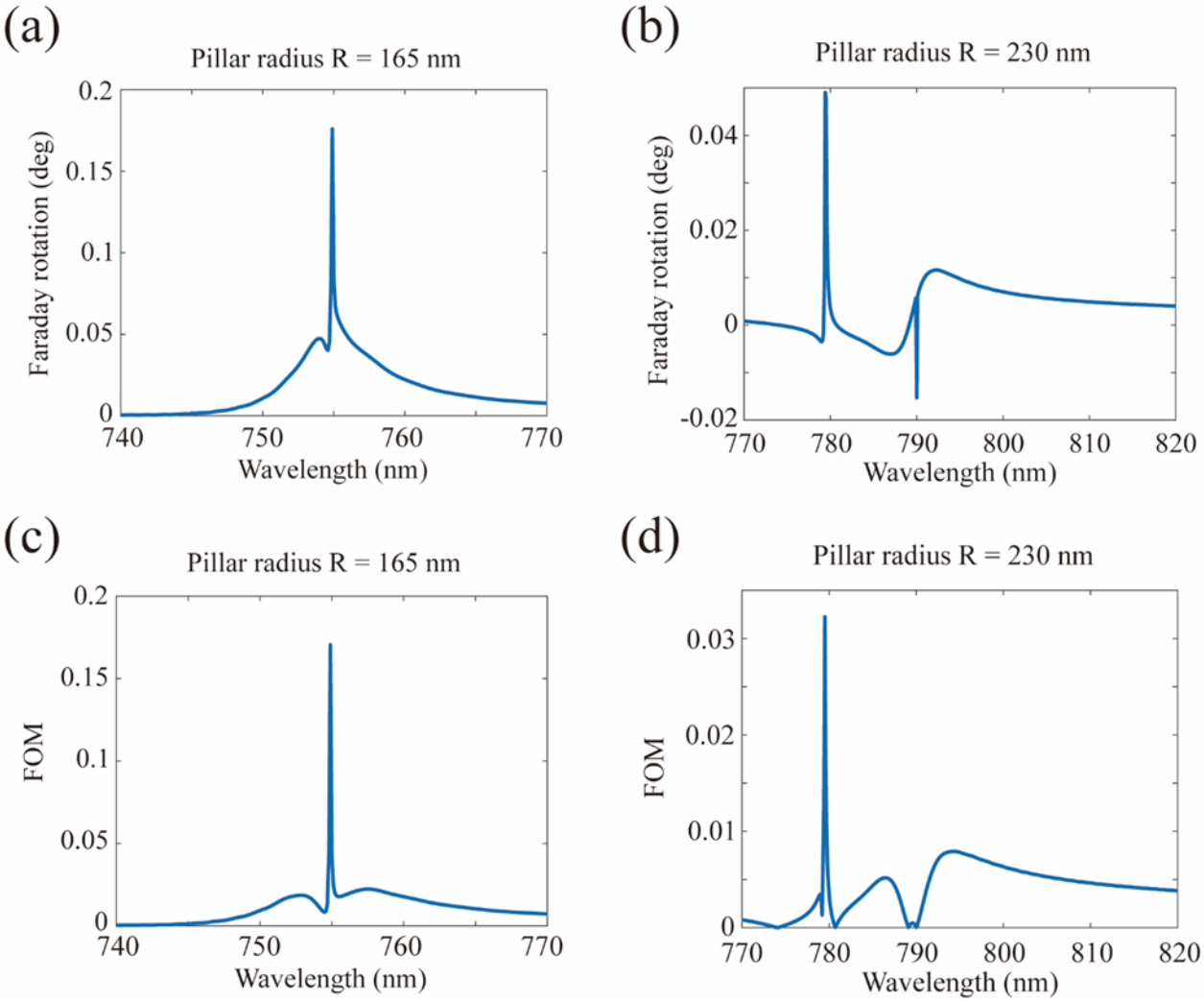

Fig. 13 – Faraday rotation angle and figure of merit (FOM) for the TE and TM guided mode resonances. (a) The Faraday rotation angle as a function of wavelength in the overlapping resonance condition. (b) The Faraday rotation angle as a function of wavelength in the spectrally separated resonance condition. (c) FOM as a function of wavelength in the overlapping resonance condition. (d) FOM as a function of wavelength in the spectrally separated resonance condition. In the overlapping resonance condition, a high Faraday rotation angle and a high FOM value are obtained at the wavelength of resonance overlapping (~755 nm), suggesting high performance of our designed device at this wavelength.

4.7 – Fabrication of EuS metasurfaces

As the new EuS deposited by our MIT collaborators, Y. Hou and Prof. J. Moodera, no longer dissolves in solvents, we updated the fabrication protocol to a lift-off process (see Fig. 14), which is simpler and more efficient than the fabrication processes presented in the previous reports. The new process only consists of four steps: electron-beam lithography writing on ZEP resist, EuS deposition by our collaborators, ZEP resist removal with remover PG, and SiO_2 deposition to embed the EuS pillars.

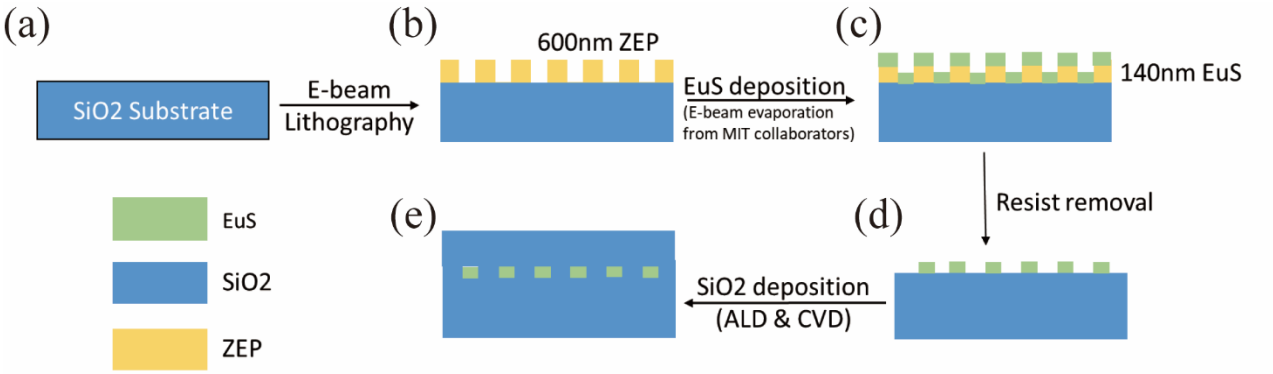

Fig. 14 – The workflow of the fabrication process. The acronyms in the parentheses refer to the fabrication tools. ALD, atomic layer deposition; CVD, chemical vapor deposition.

Fig. 15 (a) and (b) present a zoom-out and zoom-in view of the fabricated sample cross section at stage (e), respectively. Although the tilted sidewalls of the EuS pillars are an unsolved issue for all the fabrication protocols we have tried, the dimensional measurements of this new sample reveal that the lattice period, pillar thickness, and pillar radius well match our design, making these samples promising for the optical measurement. The sidewall angle of the EuS pillars in this device is ~65 degrees.

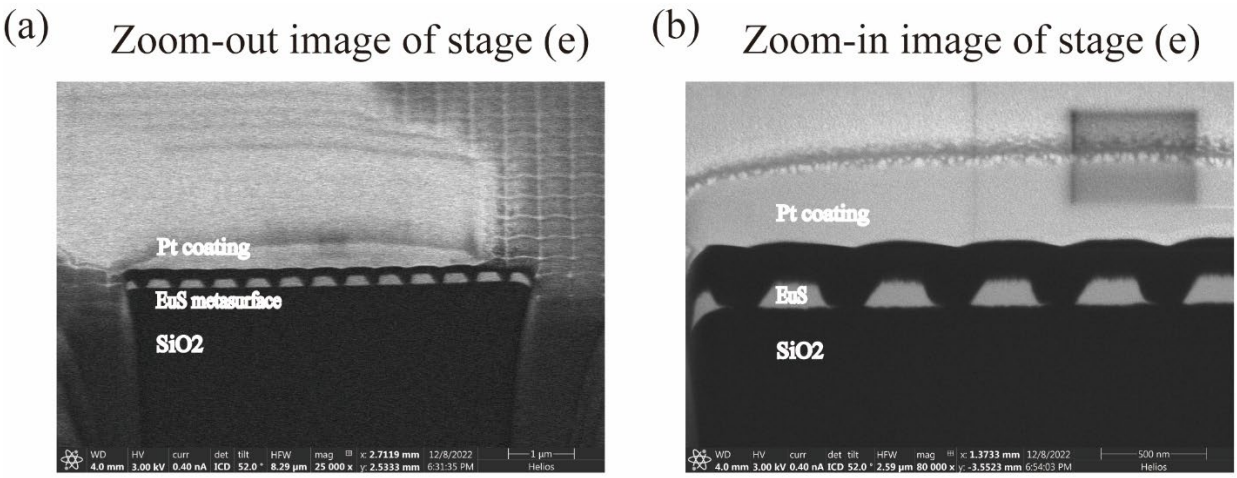

Fig. 15 Focused ion beam microscopy (FIB) images of the sample fabricated with the workflow in Fig. 14. (a) and (b) are a zoom-out image and a zoom-in image of the stage (e) of the fabrication process. The dimensions of the three geometrical parameters well match our design, and the only problem is the tilted sidewalls of the EuS pillars.

4.8 – Robustness study

Before doing optical measurement, we studied the robustness of the designed metasurface against the tilted sidewall geometry that occurs during the fabrication described above. Setting $a = 500\,nm, R = 145\,nm, L = 140\,nm$, and a sidewall angle of 65 deg, we calculated the transmission spectrum, Faraday rotation angle, and FOM for the design with tilted sidewall pillars. Material absorption is also considered in this simulation. The results are presented in Fig. 16. While the design with straight pillar sidewalls and zero absorption can reach near-100% transmittance in the overlapping resonance condition (Fig. 12 (b)), this design, which is closer to the real fabricated devices, possesses ~33% transmittance in the same condition.

In Fig. 16 (b)(c), this device possesses a maximum Faraday rotation angle of ~0.09 deg and a maximum FOM value of ~0.025, which are ~11.3 and ~3.1 times larger than their counterparts in the same-thickness uniform EuS film.

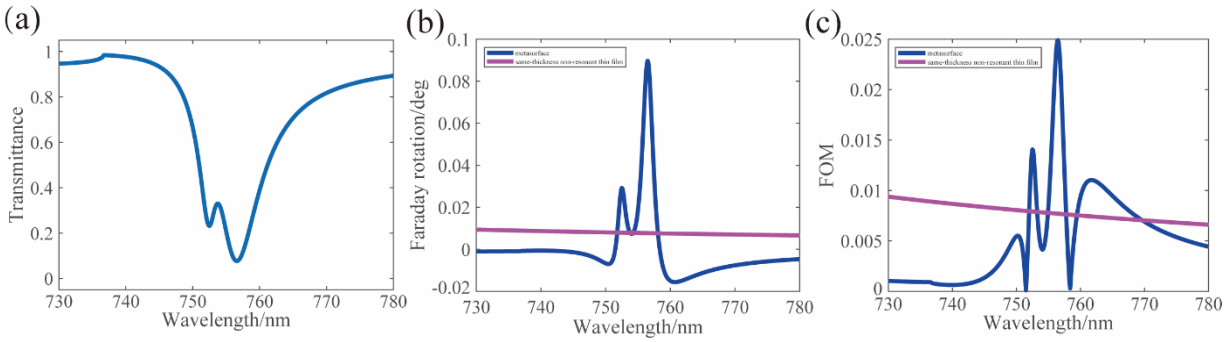

Fig. 16 – Transmittance (a), Faraday rotation (b), and FOM (c) of a structure with a tilted sidewall angle. Parameter setting: a=500 nm, R=145 nm, L=140 nm, sidewall angle=65 deg. Normal incidence is applied, and material absorption is considered. Compared to the structure with straight pillar sidewalls, the transmittance at the wavelength of resonance overlapping drops from ~100% to ~33% for the tilted pillar sidewall design. Nevertheless, its maximum FOM is still ~3.1 times larger than the same-thickness uniform EuS film, suggesting it is still worth doing the optical measurement.

4.9 – Transmittance measurements

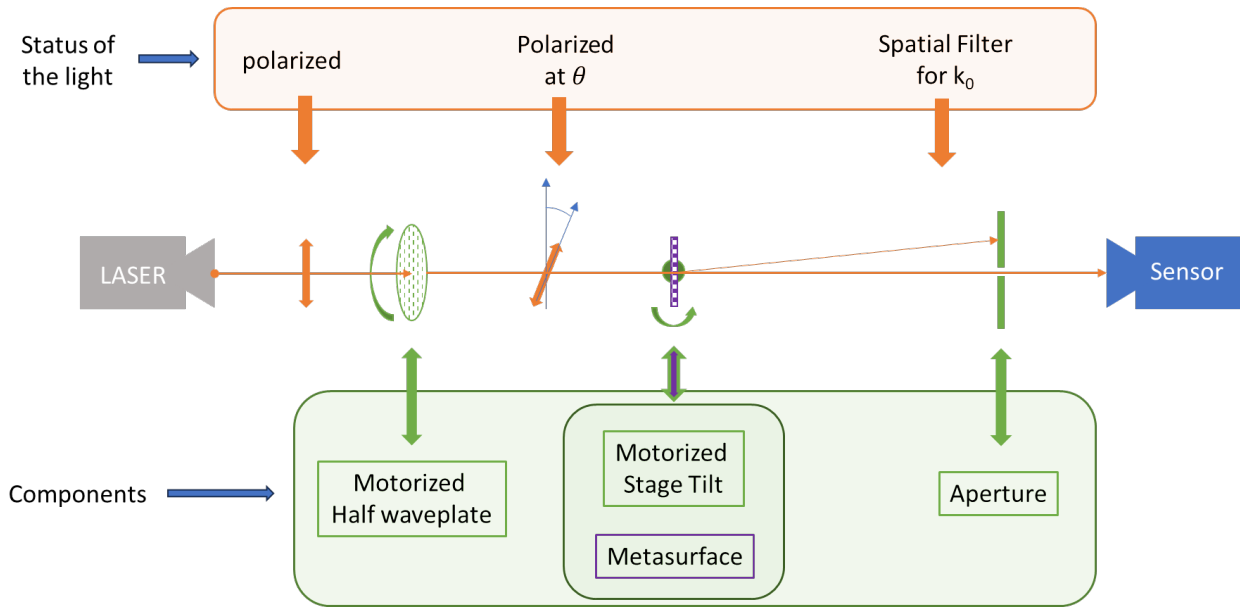

Fig. 17. Set-up for the transmittance measurement. The laser output passes through a polarizer, a half waveplate, the sample, and an aperture, and is finally collected by the sensor. This set-up has the ability to precisely change the wavelength, polarization, incident angle of the light, making it suitable for the guided mode resonance measurement.

The transmittance measurement set-up is shown in Fig. 17. The laser output passes through a polarizer, a half waveplate, the sample, and an aperture, and is finally collected by the sensor. This set-up allows for the control of multiple degrees of freedom, such as wavelength, polarization, incidence angle, etc. The stage tilt and half waveplate are controlled precisely by the motors to overcome the high sensitivity of the guided mode resonances to the incidence angle and polarization.

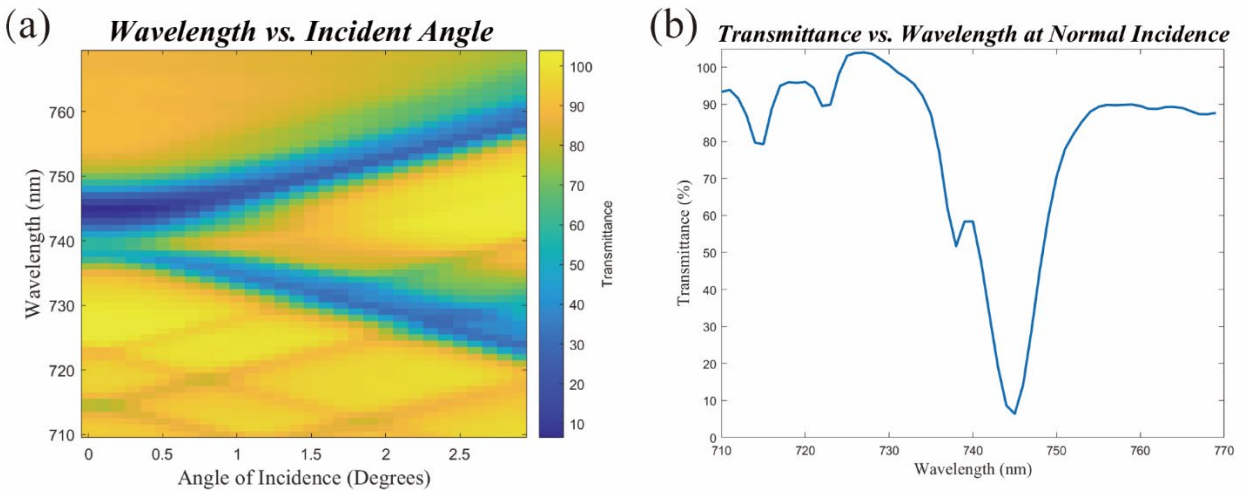

Fig. 18 –Transmittance spectra measurement. (a) The transmittance spectra map as a function of the wavelength and incident angle. It can be clearly seen that the resonances are splitting when the incident angle increases. (b) The transmittance spectrum plot when the incident angle is zero. The two resonances between the wavelength 730 nm and 755 nm and the overlapping resonance condition are our expected results and match the simulation in Fig. 11 (a) very well.

The measured transmittance spectra map as a function of the wavelength and incident angle is presented in Fig. 18 (a) for a sample with a=500 nm, R=145 nm, L=140 nm. When the incidence angle is zero, the transmittance spectrum is plotted in Fig. 18 (b). In the wavelength range between 730-755 nm, the spectrum shows two resonances and the overlapping resonance condition and matches the simulation in Fig. 16 (a) very well. When the incidence angle increases, both resonances split (see Fig. 18 (a)). Since the incident light of this measurement has both p- and s-polarizations, it makes sense that both the TE and TM guided mode resonances are affected and experience splitting when the incidence angle is not zero.

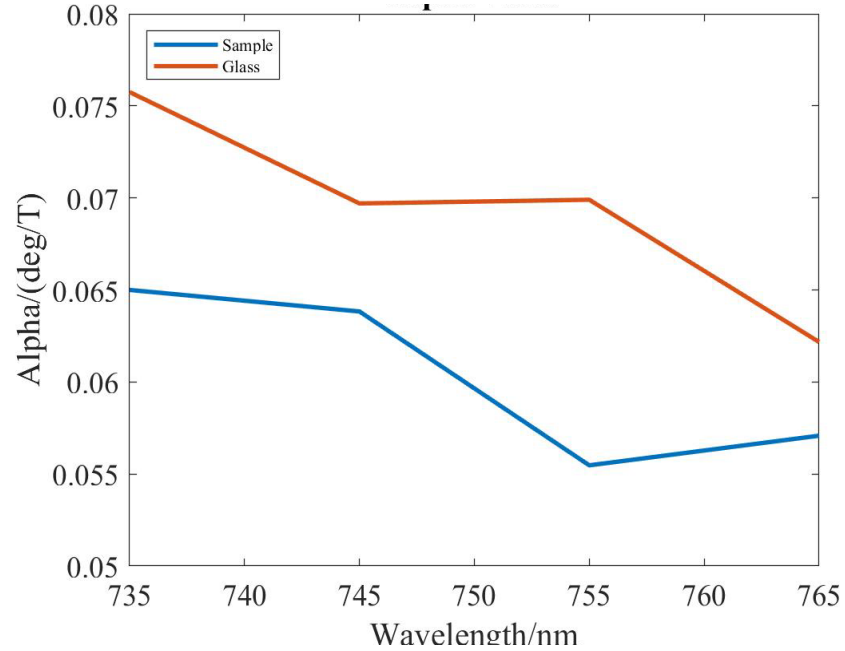

Fig.19– Alpha value spectra measurement. The alpha value α is used to characterize the strength of the Faraday effect. This figure shows the alpha value spectra of the sample and a bare glass substrate. The alpha values of the sample are always smaller than the glass substrate because the Verdet constants of glass and EuS have opposite signs.

4.10 – Faraday rotation measurements

The measurement set-up and method are presented in detail in our previous publication [M. Mereszka et al. *Applied Physics Letters* 120, 25, 2022] on this project. To characterize the strength of the Faraday effect, the alpha value α is introduced and is defined as

$$\alpha = \frac{\theta_{PR}}{B} \ . \tag{9}$$

Here θ_{PR} is the polarization rotation angle, and B is the magnetic field applied to the sample.

For each wavelength, we sampled a few different magnitudes of the magnetic field B and measure their corresponding Faraday rotation angles θ_{PR}. The alpha value α is obtained by linearly fitting θ_{PR} and B. Preliminary alpha value spectra of the sample and a bare glass substrate are plotted in Fig. 19. Note that the Verdet constants of glass and EuS have opposite signs [M. Mereszka et al. *Applied Physics Letters* 120, 25, 2022]. Therefore, their Faraday rotations are intrinsically in the opposite directions, and their alpha values also have opposite signs, which explains why the alpha value of the sample is smaller than the alpha value of the glass substrate in Fig. 19. To compare with the Verdet constants of bulk materials, we can define the "effective" Verdet constant of our EuS metasurface as

$$V_{eff} = \frac{\alpha_{metasurface}}{L_{metasurface}} \ . \tag{10}$$

Here $\alpha_{metasurface}$ is the alpha value of the metasurface layer without the substrate, and $L_{metasurface}$ is the thickness of the metasurface. Taking the wavelength 755 nm as an example, $\alpha_{metasurface} = \alpha_{sample} - \alpha_{substrate} = -0.0144\ deg/T$, and $L_{metasurface} = 155\ nm$, so we get $V_{eff} = -9.31 \times 10^4\ deg/(T * m)$. This value is ~2 times larger than the Verdet constant of bulk EuS at the same wavelength, which is around $-5 \times 10^4\ deg/(T * m)$.

In conclusion we successfully observed the high-Q and low-Q resonances and the overlapping resonance condition in the transmittance spectrum measurement. We also got a ~2 times Faraday rotation enhancement with our sample. An optimization of the Faraday rotation measurement set-up is needed to obtain more reliable results with high signal-to-noise ratios.

5. Compact integrated non-reciprocal devices

The opto-isolator based on Faraday rotation is the prototypical nonreciprocal device. This has led us to consider new mechanisms to achieve optical non reciprocity. In the course of this work, we have invented and realized a new class of optical resonators where the propagation of light is asymmetric. To achieve that mirrors are designed in such a way that the back reflected light propagates in a resonator mode different that the forward propagating light. This cascaded mode conversion leads to radically different behavior compared to standard resonators such as Fabry-Perot.

5.1 Cascade-mode conversion optical resonators

In this section we present recent work on a new resonator concept that can lay the ground to novel norn-reciprocal devices. The functionality of electromagnetic resonators can be understood from the constructive interference of waves—creating resonant modes. A crucial parameter that determines these modes is the round- trip phase $\Delta\phi$, accumulated by the field after completing one round trip in the resonator[2]. Waves that pick up a round-trip phase equal to a multiple of 2π constructively interfere with themselves and become

resonant modes of the resonator (Fig. 20a). In the case of a Fabry-Perot geometry, the resonance condition is then given by

$$2Ln\frac{2\pi\nu}{c} + 2\phi_r = 2\pi m, \tag{11}$$

where ν is the frequency of light, m is an integer number representing the index of the resonant modes of frequency ν_m, c is the speed of light in vacuum, L is the length of the resonator, n is the refractive index of the material inside the resonator, and ϕ_r is the reflection phase at the mirrors. This simple equation explains two essential properties of resonators: the existence of the fundamental mode and the appearance of a spectrum with only a discrete number of modes. The resulting frequency spectrum from Eq. (6) is then given by $\nu_m = c(m - \phi_r/\pi)/(2nL)$. Above, we ignore the properties of the mode in the transversal plane. Typically, a discrete number of orthogonal transverse modes exist for each frequency, e.g., TE_i and TM_i waves, where each transverse mode experiences a different effective index ($n_{eff,i}$). As a result, the resonant modes of a resonator generally consist of a superposition of spectra, corresponding to the various families of transverse modes (Fig. 20b). The spectra are given by:

$$\nu_{i,m} = \frac{c(m - \phi_{r,i}/\pi)}{2n_{\mathrm{eff},i}L}. \tag{12}$$

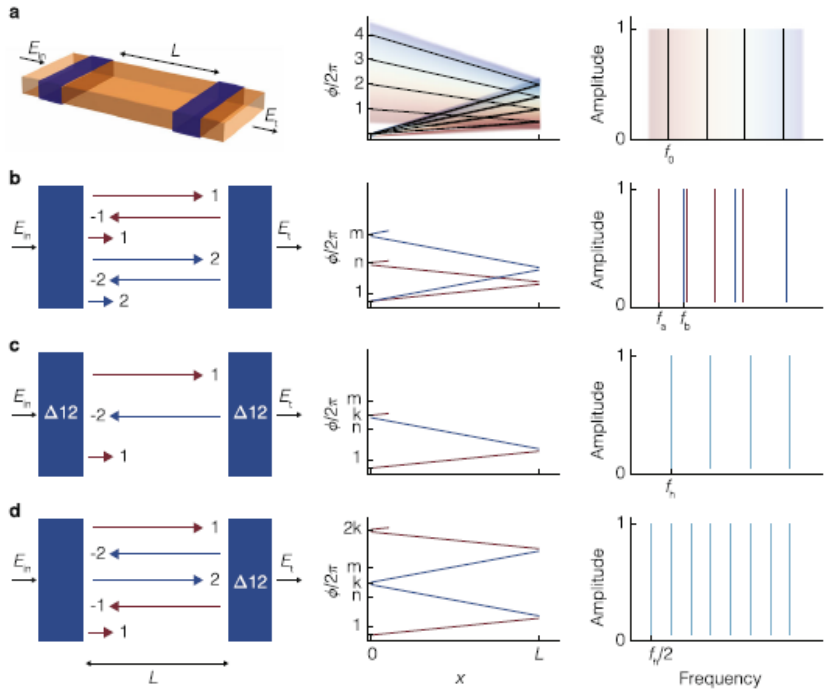

Fig. 20 The operating principle underlying cascaded-mode resonances. **a** From left to right: First, **a** visualization of traditional resonator of length L. Second, the phase shift as a function of distance x for a resonator of length L for different longitudinal modes of index m after a round trip 2L the accumulated phase is m2π. Third, the resonance spectrum, which corresponds to the frequencies for which the round-trip phase Δϕ equals a multiple of 2π. **b** In many resonators, different transverse modes contribute to different spectra because their effective refractive indices inside the resonator differ. The different effective indices determine the different slopes of the lines in the second column, which results in spectra with different fundamental modes (f_a, f_b) and mode spacings in the third column. **c** A cascaded-mode resonator (the blue regions are mode-converting mirrors) in which the two transverse modes, labeled 1 and 2, couple into one supermode, with

fundamental frequency f_h. The round-trip phase and the free spectral range are partly determined by the effective indices of mode 1 (red slope) and of mode 2 (blue slope). d A cascaded-mode resonator in which a supermode is created where both mode 1 and mode 2 circulate twice through the resonator before completing the round trip. There is one spectrum, with fundamental mode and free spectral range halved compared to c. The labels in the resonators in the first column refer to the mode conversions that take place in the blue regions: Δ_{12} implies that mode 1 is reflected into mode 2, and vice versa. Blue regions without label refer to traditional mirrors where each mode is reflected into itself.

We now introduce a new type of resonator based on cascaded mode coupling. This coupling is implemented by mode-converting mirrors that not only reflect incident waves, but also simultaneously convert them to another transverse mode profile. We illustrate this principle in Fig. 20c, d: upon reflection on the rightmost mode converting mirror, an incident wave with a particular transverse mode profile is converted into another transverse mode. When this mode returns to the leftmost mirror, another mode conversion occurs upon reflection. This non-reciprocal propagation consisting of cascade of mode conversions can be repeated as many times as the number of transverse modes supported by the waveguide. Finally, a "supermode" emerges when the wave is converted back to the original configuration of the incident mode. For resonators with N different transverse modes, the round-trip phase is given by:

$$\Delta\phi = k_0 L \xi \sum_{i=1}^{N} n_{\mathrm{eff},i} + \phi_{r,\mathrm{tot}}. \qquad (13)$$

Here k_0 equals $2\pi/\lambda_0$ with λ_0 the vacuum wavelength, $\phi_{r,\mathrm{tot}}$ is the sum of all reflection phases, and ξ is the parameter that encodes whether the contributing transverse modes appear once ($\xi = 1$) or twice ($\xi=2$) in the chain. The round-trip phase is thus no longer merely determined by the length of the resonator and the refractive index but also by the number of coupled transverse modes. The corresponding resonance condition is

$$\nu_m = \frac{c\left[m - \phi_{r,\mathrm{tot}}/(2\pi)\right]}{L\xi \sum_{i=1}^{N} n_{\mathrm{eff},i}}. \qquad (14)$$

The free spectral range is thus set by the denominator which represents the sum of the round-trip optical paths of the different cascaded modes $L\xi \sum_{i=1}^{N} n_{\mathrm{eff},i}$ rather by $2n_{\mathrm{eff},i}L$ as in a conventional resonator. Next, whereas traditional resonators feature an incoherent superposition of different spectra, each corresponding to a different transverse mode, cascaded-mode resonators exhibit just one superspectrum (Fig. 20 c, d). This analysis is independent of how the mode conversions are realized. For instance, in the context of transverse modes in waveguides, a mode converter can be implemented using a specific refractive index variation (blue regions in Fig. 20 a–d).

An interesting feature of cascaded-mode resonances, in agreement with the geometrical model described above, is the modification of the free spectral range $\Delta\nu$, given by:

$$\Delta\nu = \frac{c}{\xi \sum_{i=1}^{N} n_{g,i} L}, \qquad (15)$$

where $n_{g,i}$ is the group index of transverse mode i at frequency ν.

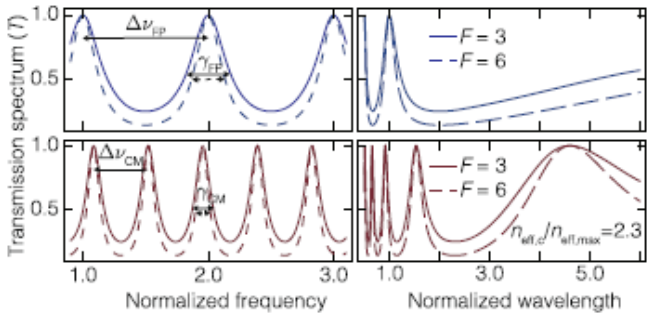

Fig 21 The spectral properties of cascaded-mode resonances. The spectra of a traditional resonator compared with the spectra of a cascaded-mode resonator versus frequency (left) or wavelength (right). The blue and red spectra respectively correspond to conventional resonators and cascaded-mode resonators with $n_{eff,c}=n_{eff,max}=2.3, \phi_{r,tot}=1.5\pi$. The solid and dashed lines correspond to a resonator's finesse equal to 3 and 6, respectively. Note the reduction of the free spectral range Δν and linewidth γ when several transverse modes are coupled.

Two other crucial spectral parameters can be engineered in a cascaded mode resonator by controlling the round-trip phase: the linewidth γ and the quality factor Q (Fig. 21). Unlike the free spectral range, the linewidth and the quality factor depend on the round-trip losses. Not only the spectral properties but also the temporal and spatial properties of these modes can be engineered by using cascaded-mode coupling. The intracavity power build-up and the intracavity power build-up time both scale proportionally to the number of coupled modes. While the intensity of longitudinal modes in traditional resonators exhibits a simple standing-wave profile, the intensity profile in a cascaded-mode resonator will have a more irregular profile, potentially with many different local minima and maxima.

A unique spatial property of cascaded-mode resonators is that the propagation constant of a supermode depends on the propagation direction. This phenomenon is shown in its most straightforward implementation in Fig. 20c. When a field with transverse profile of mode 1 is incident on the left side of this resonator, a cascaded mode will exist with wave vector $k = k_{0neff,1}$ propagating from left to right, and a wave vector $k = k_{0neff,2}$ propagating from right to left. Due to the distinct propagation constants in opposite directions, directional nonlinear optical effects can occur in the resonator since the phase matching conditions may only be satisfied in one direction. The directionality could also give additional control over chiral, optomechanical, or quantum mechanical interactions inside the resonator. A final property of cascaded-mode resonances that deserves special attention is the existence of mode-independent spectra. Indeed, different transverse modes at the input may excite the same resonance, i.e., a mode-independent resonance. As an example, in the resonators of Fig. 20c–d the transmission spectrum (third column) is the same for the two incident transverse modes (1 and 2). The mode-independent behavior of cascaded-mode resonators is a unique transmission characteristic, a feature verified experimentally in Fig. 22. This contrasts with traditional resonators, where different transverse modes exhibit different transmission spectra. Based on this property, it becomes possible to manipulate modes with different spatial profiles in an identical way using only one resonator.

5. 2 Experiments

We experimentally realize the proposed cascaded-mode resonators using the silicon-on-insulator (SOI) platform at telecom wavelengths (1550 nm). In our on-chip implementation, the cascaded modes have distinct transverse profiles TE_i, an in-plane polarization, and propagate along waveguides rather than in free space. The SOI

platform offers design flexibility in engineering the properties of the mode converters (reflection phase and magnitude), as well as the propagation properties of all modes participating in the cascade, such as their effective indices $n_{\mathrm{eff},i}$.

The device geometry is shown in Fig. 22 a,b together with scanning electron microscope (SEM) pictures of the fabricated structures. Materials. In general, each device consists of three main optical components: in- put/output waveguides that couple and guide light of chosen transverse modes to and away from the mode-converting resonators; a multi-mode waveguide section of length L_{wg} in which the cascaded modes are confined; specialized corrugated Bragg reflectors located on either side of the multi-mode waveguide that reflect one transverse mode into another. While, as described theoretically above, the number of conversions in a cascaded mode is only limited by the number of available transverse modes, we restrict our experimental demonstration to cascaded-mode resonators of the type shown in Fig. 20 that couple the two distinct transverse modes TE_0 and TE_2.

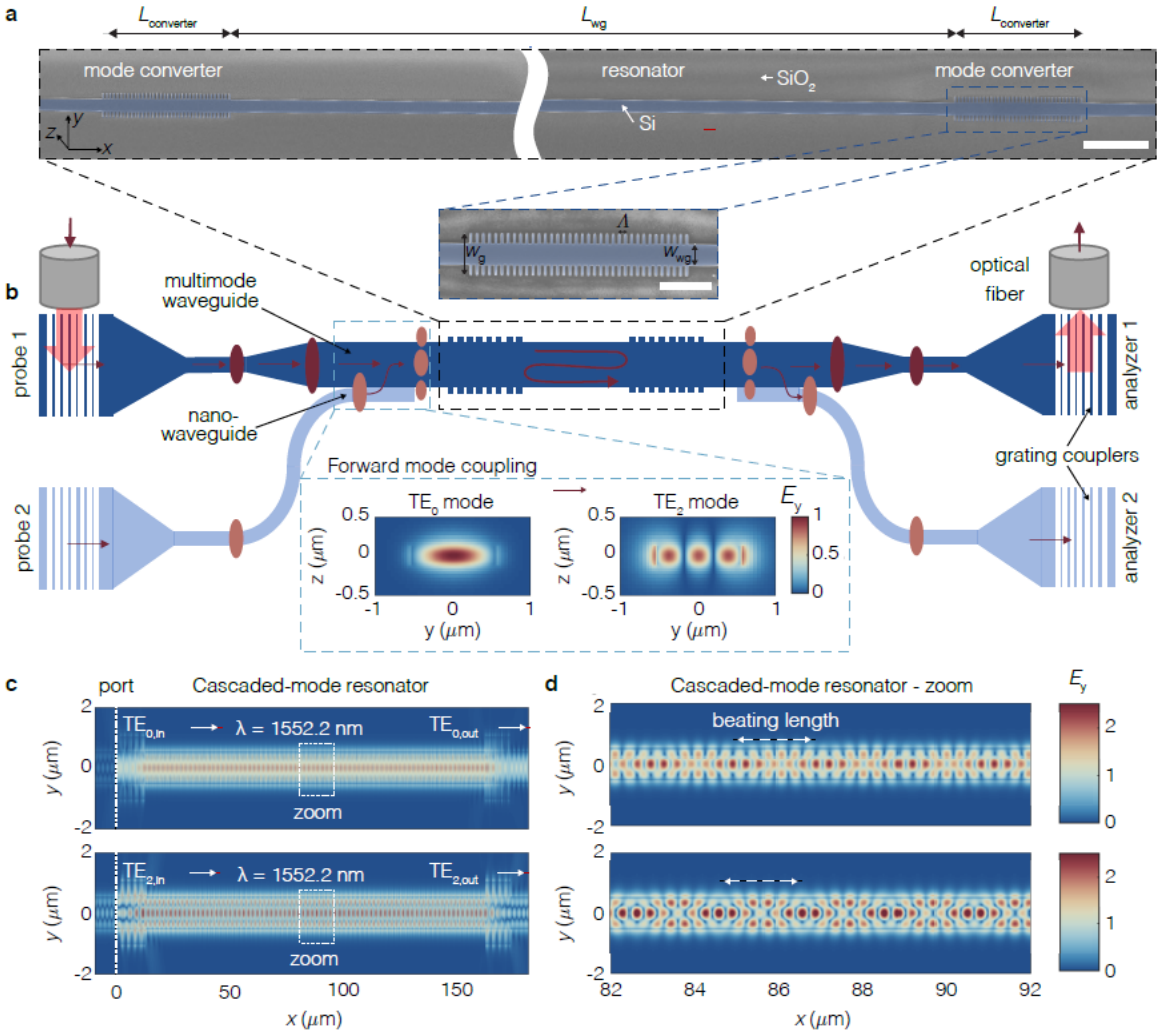

Fig. 22 | Experimental realization of cascaded-mode resonators in integrated photonics. a SEM pictures of the cascaded-mode resonator show two-mode converters connected via a multimode waveguide of width w_{wg} and length L_{wg}. Multimode waveguides located before and after the resonator guide telecom light into and outside the resonator. The mode converters are realized by corrugating the silicon waveguide laterally into the shape of a rectangular grating of periodicity Λ and width w_g. Scalebar = 5 μm and 2μm (inset). The periodicity Λ is chosen such that the phase-matching condition is satisfied for contra-directional coupling. The entire photonic circuit ridge is buried into a silica

layer. b Schematic of the device shows three different sections: 1. two input waveguides (left) that allow to probe the resonator with either TE0 (upper) or TE2 (lower), 2. the resonator region consisting of the multimode waveguide enclosed by the two mode converters, and 3. two analyzer waveguides which transmit the output of the resonator into two spatially separated locations, depending on its transverse profile TE_0 (upper) or TE_2 (lower). Probe 1 excites the TE_0 mode in the top waveguide. Probe 2 excites the TE_0 in the lower waveguide. This mode is converted into the TE_2 mode in the top multimode waveguide prior to the resonator via the forward-mode coupler, which operates on the principle that the effective index of the TE_0 mode in the nano-waveguide corresponds to the effective index of the TE_2 mode in the multimode waveguide. Similarly, analyzer 1 and analyzer 2 measure TE_0 and $_{TE2}$ modes, respectively. Spatially, the coupling occurs at the location where the nanowaveguide is in the immediate vicinity of the multimode waveguide. c Full-wave simulations of the telecom fields inside the cascaded-mode resonator demonstrate that self-consistent solutions of the round-trip condition occur at the same input wavelength for two distinct transverse modes $_{TE0}$ (upper) and TE_2 (lower). d Zoom into marked white region inside the resonator reveals the hybrid nature of the cascaded modes that arise as a superposition of counter propagating TE_0 or TE_2 modes with a characteristic beating length that does not depend on the input probe field.

Their transverse mode profiles are shown in the inset of Fig. 22 b. Consequently, the width of the waveguide in the cavity region (w_{wg} = 1.07 μm) was chosen such that it cuts off all transverse modes of a higher order than TE_2. In addition, the grating period Λ of the mode converters is chosen as to satisfy the phase-matching condition and provide the necessary momentum for the mode conversion to occur on the reflected wave: $2\pi/\Lambda = \Delta\beta_{12} = \beta_1 + \beta_2$, with $\beta_1 = \beta_{TE0} = n_{eff,TE0}\,\omega_0/c$ and $\beta_2 = \beta_{TE2} = n_{eff,TE2}\,\omega_0/c$ the propagation constants of the two coupled modes. This type of coupling is typically referred to as contra-directional coupling.

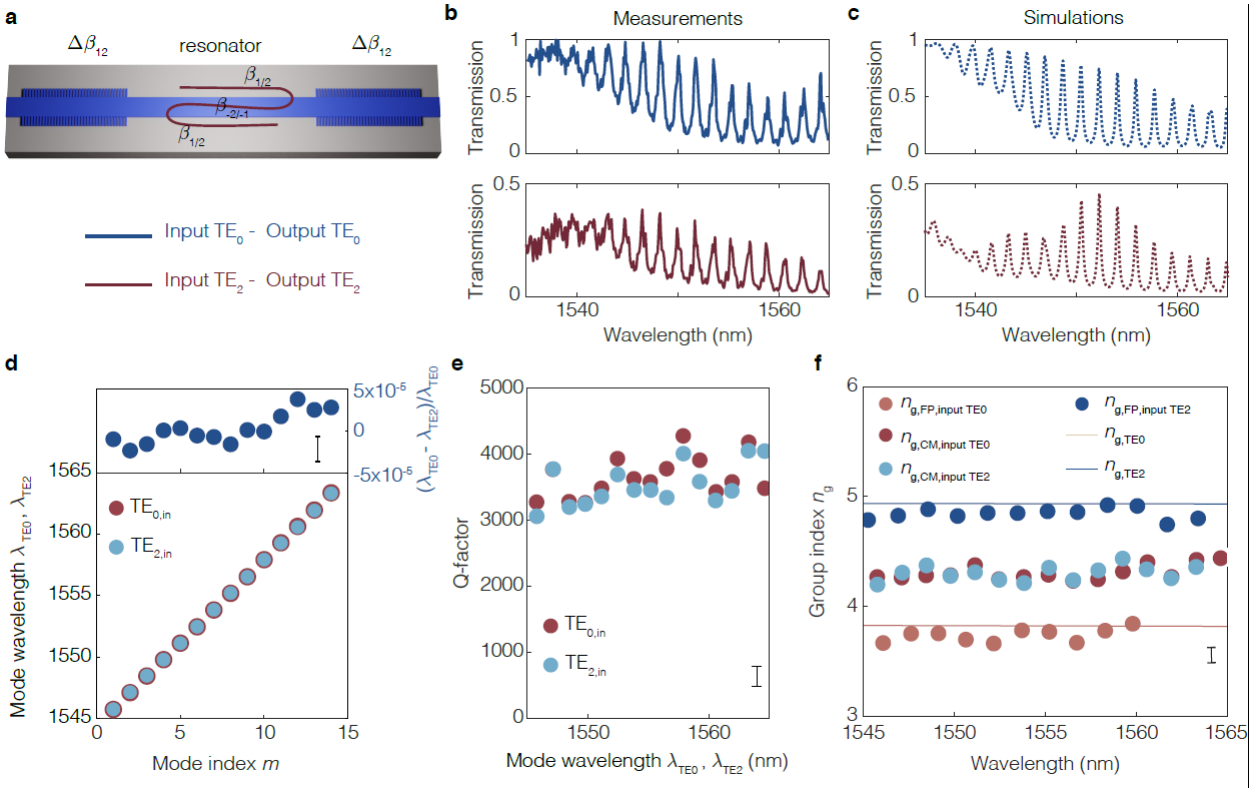

Fig. 23 Transmission spectroscopy of cascaded-mode resonators. a A cascadedmode resonator, where a reflection at both the left and the right Bragg mirror results into a conversion of the transverse mode from TE_0 to TE_2 and vice-versa. b The measured transmission spectra of the cascaded-mode resonator exhibit resonances regardless of whether TE_0 or TE_2 is

incident onto the resonator. c Simulated transmission spectra reproduce well the measurements. More measurement and simulation results are provided in the Supplementary Material. d–f Characteristic parameters of the cascaded-mode resonator extracted from the experimental transmission spectra. d The mode-independent character of cascaded-mode resonators is demonstrated by the fact that the resonant wavelengths of the cavity modes coincide in frequency (and wavelength), regardless of whether the resonator is probed by a TE_0 or TE_2 mode. The relative experimental mismatch between their resonant wavelengths is below $4 \times 10{-}5$, for all 13 considered modes, which is comparable to the experimental noise (upper panel). e Also the quality factors of the cascaded-mode resonator are mode-independent, as they coincide within the experimental error, regardless of whether the cascaded modes are excited by TE_0 or TE_2 inputs. The experimental error is calculated from the error of the fit of the resonance peaks. f In cascaded-mode resonators, the propagation constants change magnitude at each reflection off a mode-converting Bragg mirror, and the group indices of cascaded-mode (CM) resonances are equal to the arithmetic mean of conventional Fabry-Perot (FP) resonances in the same multimode waveguide. This property is confirmed experimentally, with TE_0 modes having a group index of 3.75, TE_2 modes having a group index of 4.85 and cascaded modes having a group index of 4.3. Full lines represent calculated group.

We now demonstrate in experiments and simulations the most evident signatures of cascaded-mode resonators: the mode-independent spectrum with modified spectral parameters. The symmetric cascaded-mode resonator of Fig. 20c provides resonant confinement to input modes that correspond to either TE_0 or TE_2 transverse modes and has the same transmission spectrum for either input. We confirm this computationally in Fig. 22c, where we report the simulated field profile of the same cascaded-mode resonator for the two possible inputs and find a locally enhanced field inside the resonator in both cases. Moreover, the hybrid nature of the near-infrared cascaded mode inside the resonator becomes apparent in the zoom-in of the spatial profile shown in Fig. 22d. The field profile can be decomposed into a superposition of counter propagating TE_0 and TE_2 waveguide modes that exhibit, as expected, the same beating length for both inputs (marked by the white arrow). We demonstrate this property experimentally by transmission spectroscopy and contrast it with two test Fabry-Perot resonators that employ standard mirrors and provide cavity confinement to only one of TE_0 or TE_2 modes. The experimental results are shown for the three cases in Fig. 23 a-c. We find that cavity modes appear, as expected, for both TE_0 and TE_2 modes in the case of the cascaded-mode resonator only. Moreover, the experimental results are well-reproduced by our simulations. Cavity modes appear only for one of the two modes for the conventional Fabry-Perot resonators, while light is simply transmitted for the other modes.

Next, we analyze the resonator properties of the cavity modes associated with the cascaded-mode resonators compared to the conventional Fabry-Perot modes in Fig. 23d-fFirstly, we show in Fig. 23d that the intra-cavity modes of the cascaded-mode resonators excited by the two inputs (TE_0 or TE_2) coincide in frequency. We experimentally find a negligible relative deviation between the two sets of resonant wavelengths of $\approx 4\text{x}10^{-5}$. Furthermore, the quality factors of the two sets are approximately equal, as shown in Fig. 23e. Finally, the group index of the cascaded modes is approximately equal to $n_g = 4.3$, regardless of whether they are excited by TE_0 or TE_2. In contrast, the group index of the Fabry-Perot modes are equal to $n_{g,TE0} = 3.75$ and $n_{g,TE2} = 4.85$ (Fig. 23f). This result confirms once more the cascaded-mode character of the measured spectra, particularly because the group index is approximately the arithmetic mean of the group indices of the participating transverse modes.

5.3 Prospects for non-reciprocal devices

The cascaded-mode resonator has a broken mirror-symmetry, which lays the foundation for broken reciprocity.

However, the mechanism is a bit more subtle; it is known that reciprocity can only be broken in one of the following 3 ways: by including materials with magneto-optic interactions, nonlinear interactions, or explicit time-dependent material parameters. Now, a nonlinear material in itself is not enough to break the reciprocity of a system (e.g. about a traditional nonlinear cavity). The crux of the story now is that the cascaded-mode resonator can be made non-reciprocal by including a nonlinear material inside the cavity because the nonlinear material can be tailored to only be phase matched with the mode propagating in one the two directions. This would create broken reciprocity behavior.

Papers

M.L. Meretska, F. H. B. Somhorst, M. Ossiander, Y. Hou, J. Moodera, and F. Capasso "Measurements of the magneto-optical properties of thin-film EuS at room temperature in the visible spectrum." *Applied Physics Letters* **120**, 25 (2022). Data made available to the public https://refractiveindex.info/?shelf=main&book=EuS&page=Meretska.

F. H. B. Somhorst, M.L. Meretska, M. Ossiander, Y. Hou, J. Moodera, and F. Capass**o** " Magneto-optical properties of e-beam evaporated EuS films for room temperature applications" *Proceedings of the European Conference on Integrated Optics (ECIO)* 2023 https://www.ecio-conference.org/2023-proceedings/

Vincent Ginis, Ileana-Cristina Benea-Chelmus, Jinsheng Lu, Marco Piccardo, and Federico Capasso "Resonators with tailored optical path by cascaded-mode conversions." *Nature Communications* **14,** 495 (2023)

Honors – Federico Capasso

2023 Selected as Citation Laureate, one of 23 worldwide in science, by the Institute for Scientific Information (ISI)™ at Clarivate; "for pioneering research on photonics, plasmonics, and metasurfaces, as well as contributions to the invention of and improvements on the quantum cascade laser." https://clarivate.com/news/clarivate-unveils-citation-laureates-2023-annual-list-of-researchers-of-nobel-class/

2021 Ives Medal and Jarus Quinn Prize of Optica "for seminal and wide-ranging contributions to optical physics, quantum electronics and nanophotonics" The highest award of Optica (formerly OSA)

26th Micro-optics Conference Award "for pioneering contributions to quantum cascade lasers, plasmonic and metamaterials" Hamamatsu City, Japan

Participants

- Graduate students: Zhongpeng Sun
- Undergraduate students: F. H. B. Somhorst.
  Received a Master degree at Twente University based on the magneto optic work here reported
- Postdocs: Maryna Meretska, Christina Benea Chelmus, Marcus Ossiander, Jinsheng Lu

Collaborators

- Prof. Jagadeesh Moodera (MIT), Y. Hou (MIT)
- Prof. Vincent Ginis, Free University of Brussels and Harvard University

- Marco Piccardo, Italian Institute of Technology

Final Performance Report
AFOSR Grant Number: FA9550-19-1-0352
High-index dielectric metasurfaces for enhanced magneto-optics
Reporting Period: 09/15/2019– 09/14/2023
Program Manager: Lt. Col Wooddy Miller

PI: Prof. Federico Capasso
John A. Paulson School of Engineering and
Applied Sciences, Harvard University
Pierce Hall 205A
29 Oxford St.
Cambridge MA 02138
Tel. 617-3847611
Email: capasso@seas.harvard.edu

1. Goals

The magneto-optical effect lies at the heart of many non-reciprocal devices such as isolators and circulators. Since it is a very weak effect that linearly scales with the size of the magneto-optic material, the resulting devices tend to be bulky. This makes free-space applications cumbersome, but moreover precludes the realization of highly integrated, field-deployable devices. The goal of this work is to design, fabricate and test resonant metasurfaces to enhance the magneto-optic effect in low-loss dielectrics. Furthermore, we endeavor to employ the insight from this proof-of-concept research to experimentally realize waveguide-based non-reciprocal devices such as on-chip optical isolators. Various approaches were utilized. First the exploration of promising but little studied magneto-optical materials such as Europium Sulfide (EuS) with a potentially large Verdet constant. In parallel resonant effects that have the potential advantage of enhancing the Faraday rotation with greatly reduced bulk were studied. This includes on-chip magneto-optic devices based on metasurfaces that enhance polarization rotation. Here the new working principle is based on guided wave resonance to enhance the Faraday rotation. This resonance occurs in suitably designed EuS metasurface 2D photonic crystals. The third approach focused on exploring new nonreciprocal design concepts. The investigation concentrated on structures dubbed cascaded mode converters that enabled the demonstration of new resonators, with performance radically different from Fabry-Perot devices

2. Accomplishments

- Investigation of properties (optical, X-ray diffraction) of Europium Sulfide (EuS) films for novel magneto-optical devices
- Guide-wave resonance metasurface magneto-optical device: design, simulations, fabrication, and measurements
- New nonreciprocal devices: cascaded mode resonators. Design, simulations, fabrication, and measurements

3. Metasurface based magneto-optical devices

3.1 - The magneto-optic effect

The most important MO effects (Faraday and Kerr effects) occur due to the splitting of energy levels of a MO material in an external magnetic field [*AK Zvezdin, VA Kotov, Modern magnetooptics and magnetooptical materials*, Taylor&Francis, 1997]. The ground and excited states of such systems become nondegenerate for light carrying distinct spin angular momenta. The MO material exhibits different refractive indices for left and right circularly polarized light:

$$n_{\pm}(\omega) \approx n(\omega) \pm \frac{dn}{d\omega}\frac{eH}{2mc} \tag{1}$$

where $n(\omega)$ is the refractive index in the absence of the field H, n_+ and n_- are the refractive indices of left and right circularly polarized light, respectively, e and m are the electron charge and mass and c is the speed of light in vacuum. Linearly polarized light propagating in this medium along the z-axis has the form

$$E = \frac{1}{2}E_o e^{-i(wt-2\pi nz/\lambda)}[\hat{x}\cos\theta + \hat{y}\sin\theta] \tag{2}$$

where $\hat{x}$ and $\hat{y}$ are the unit vectors along the x- and y-axis.
When light travels a distance L inside the MO crystal, the polarization of light rotates by an angle:

$$\theta = \frac{k(n_+ - n_-)L}{2}, \tag{3}$$

where k is the wavevector of the incident light, L is the thickness of the MO medium and n_+, n_- are the refractive indices along the x and y axis, respectively.
This expression can be rewritten using the Verdet constant V, which determines the angle of rotation per unit length and per unit field strength B:

$$\theta = VBL. \tag{4}$$

The MO effect radically differs from optical activity associated with chiral media. When light travels multiple times back and forth through a MO material, the polarization rotation angle accumulates. This effect occurs due to broken time-reversal symmetry imposed by the magnetic field. Thus, the device is inherently nonreciprocal. Hence, large polarization rotation angles can be achieved by cycling through the same volume multiple times.

The effect of polarization rotation has been used in a wide variety of practical applications. An optical isolator (diode) is one of the basic devices that exploits this effect in MO materials, and an important building block. The schematic of a Faraday isolator is shown in Fig. 1. This device allows light to propagate only in one direction while blocking it in the opposite direction. It consists of a MO material placed in between two polarizers. The main axes of these polarizers are rotated by 45 degrees with respect to each other. Typically, a permanent magnet is placed around the MO material.

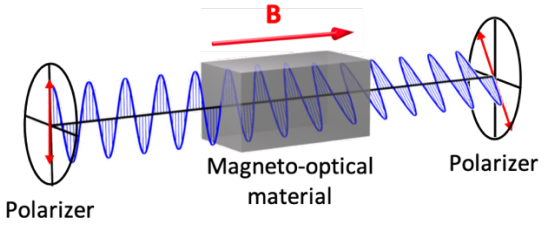

Fig. 1 - Schematics of a conventional optical isolator. The polarization of light is rotated by 45 degrees when light propagates through the MO material. A pair of polarizers ensures that light can be transmitted only in one direction.

Light traveling in the forward direction becomes linearly polarized by the input polarizer. The MO material rotates the polarization of light by 45 degrees. A second polarizer oriented at 45 degrees lets the rotated light pass. However, when light travels in the opposite direction, it becomes polarized at 45 degrees by the second polarizer and the MO material rotates it by an additional 45 degrees. The resulting polarization is perpendicular to the axis of the input polarizer, and therefore backward propagating light is blocked.
MO devices that exploit the Faraday roation are typically long and bulky. We searched therefore for physical mechansims that would allow us to reudce length and overall size and for MO materials with large Verdet constant.

For MO material we chose Europium Sulphide (EuS). This material posseses a number of advantages: a high Verdet constant in the visible spectral range (superior to TGG), low absorption and it can be deposited via thermal evaporation. The latter is of particular importance for the fabrication aspect of this work, as described below. The material, desposited by e-beam evaporation, is grown by Prof. Jagadeesh Moodera (MIT), as part of a collaboration with our group

3.3 Characterization of Europium sulfide: ellipsometry, x-ray diffraction and Verdet constant measurements

A spectroscopic ellipsometer (J. A. Woollam V-VASE32) was used to measure the refractive index of EuS in the visible spectral range. We fabricated two samples (Fig. 2) for these measurements. The first sample consists of a 20 nm thick Alumina layer deposited on the 0.5 mm thick Si substrate. The second sample consist of three layers where 50 nm thick EuS is sandwiched in between two 20 nm layers of Al_2O_3. These two layers are deposited to protect EuS from oxidation and to ensure good adhesion to the substrate. Deposition of Al_2O_3 on Si was performed simultaneously for both samples. Refractive index of Al_2O_3 is obtained from the first sample, and fed into the model that is used for sample with EuS layer. Real and imaginary parts of the refractive index measured for EuS are plotted in Fig. 4.

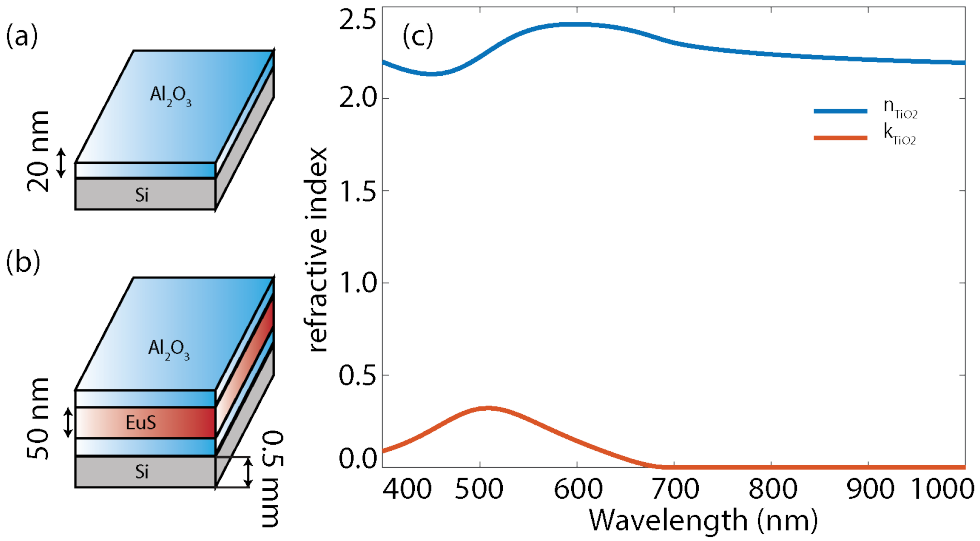

Fig. 2 - Refractive index measurement of EuS using ellipsometry. (a): Sample structure fabricated for measurement of Al_2O_3 layer refractive index. (b): Sample structure used for EuS refractive index measurements. 20 nm thick Al_2O_3 layers are added to ensure adhesion of EuS and prevent it from oxidation. (c): Real and imaginary part of refractive index for EuS extracted from ellipsometry measurements.

To confirm the purity of the material we performed x-ray difraction (XRD) analysys of the EuS powder used in the fabrication. The XRD spectrum is shown in Fig. 3. We found that peaks of the measured spectrum are in excellent correspondance to EuS XRD pattern available in crystalographyc databases.

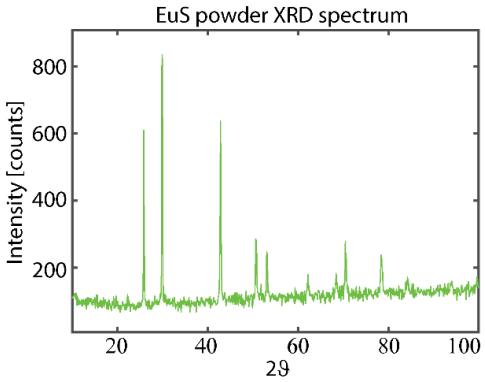

Fig. 3 - XRD measurement of EuS powder. Peaks show excellent agreement with the crystallographic database and confirm the purity of the used material.

To determine the Verdet constant of the EuS we built a custom setup for Faraday rotation measurements. We fabricated samples with 1 μm thick EuS on 0.5 mm thick quartz glass. Considering that glass is 2 orders of magnitude thicker than EuS, its polarization rotation action on light should be taken into accout.

As a first step we measured Verdet constant of quartz glass without EuS layer. Measured data are plotted in Fig. 4. The Verdet constant of glass is extracted from this measurement and is V_{Glass}=1.58±0.02 rad/mT. ($V_{pyrex} = 3\ \frac{rad}{mT}$ and $V_{SF57} = 20\ \frac{rad}{mT}$ at λ=632 nm). We measured the polarization rotation of quartz glass with EuS layer. The results of the measurements are shown in Fig. 6. The rotation caused by EuS layer can be calculated as

$$\theta_{EuS} = \theta_{glass} - \theta_{EuS\ on\ glass}. \qquad (5)$$

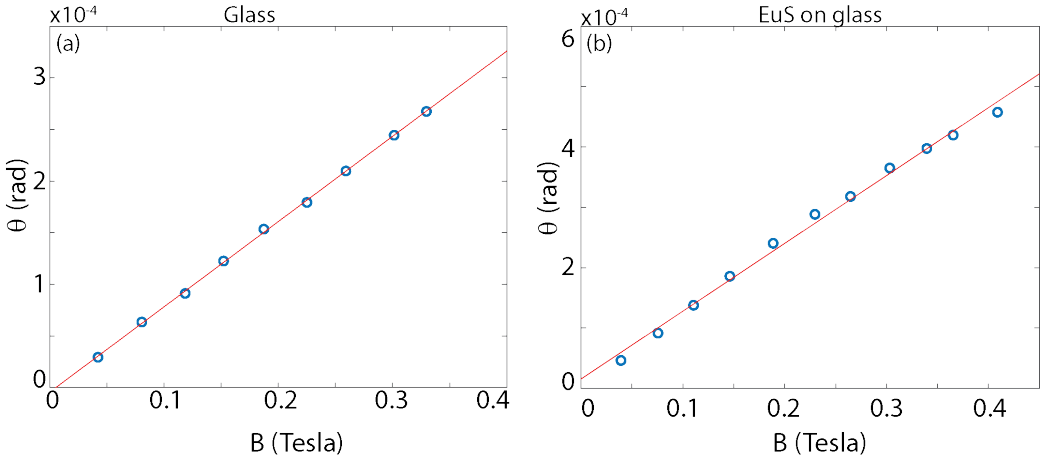

Fig. 6 - Verdet constant measurements. (a) Polarization rotation angle as a function of applied magnetic field for glass sample. (b) Polarization rotation angle as a function of applied magnetic field for glass sample with 1 μm thick EuS layer. Red lines in both images are linear fits to the data.

The angle of rotation for EuS on glass is subtracted from the angle of rotation for glass substarte, because the Verdet constant of EuS has negative sign in this wavelength region. Once the angle of rotation is known we obatin the Verdet constant of EuS to be $V_{EuS} = 2000 \pm 17\ \frac{rad}{mT}$. at room temperature [M.L. Meretska, et al. *Applied Physics Letters*, 120, 25 (2022)].

4. Guide-wave resonance metasurface magneto-optical device

4.1 – Metasurface-based free-space Faraday isolator

Some dielectric materials, such as Terbium Gallium Garnet (TGG), naturally possess a relatively high Verdet constant. TGG is commercially used in an optical isolator in the visible spectral range. Despite its relatively high Verdet constant, the resulting device dimensions are still in the order of tens of centimeters because MO effects are intrinsically weak. We aim to design metasurfaces using resonant structures based on EuS to allow for a more compact device at the micrometer scale.

The principle of miniaturizing the device based on EuS-based resonant metasurfaces is to trap the light inside the metasurface and accumulate the polarization rotation of the light through travelling back and forth multiple times. Note that the polarization rotation will keep accumulating and not be cancelled out during one back-and-forth cycle because of the non-reciprocal nature of MO effects [A K Zvezdin & V A Kotov,*Modern magnetooptics and magnetooptical materials*, 1997]. Therefore, with this metasurface, incident light experiences enhanced Faraday rotation at the resonance frequency compared to when it passes through a uniform film of the same material. However, resonances are usually accompanied by strong transmission and reflection changes so careful design is necessary to obtain a high transmittance at the resonance frequency. Additionally, a high quality factor (Q factor) is preferred because it indicates stronger light trapping within the metasurface, leading to a longer back-and-forth travel distance of light, and consequently, a larger Faraday rotation. In the next section, we will be studying a metasurface that is based on a EuS lattice (Fig. 7 (a)), along with the guided mode resonances that occur within it.

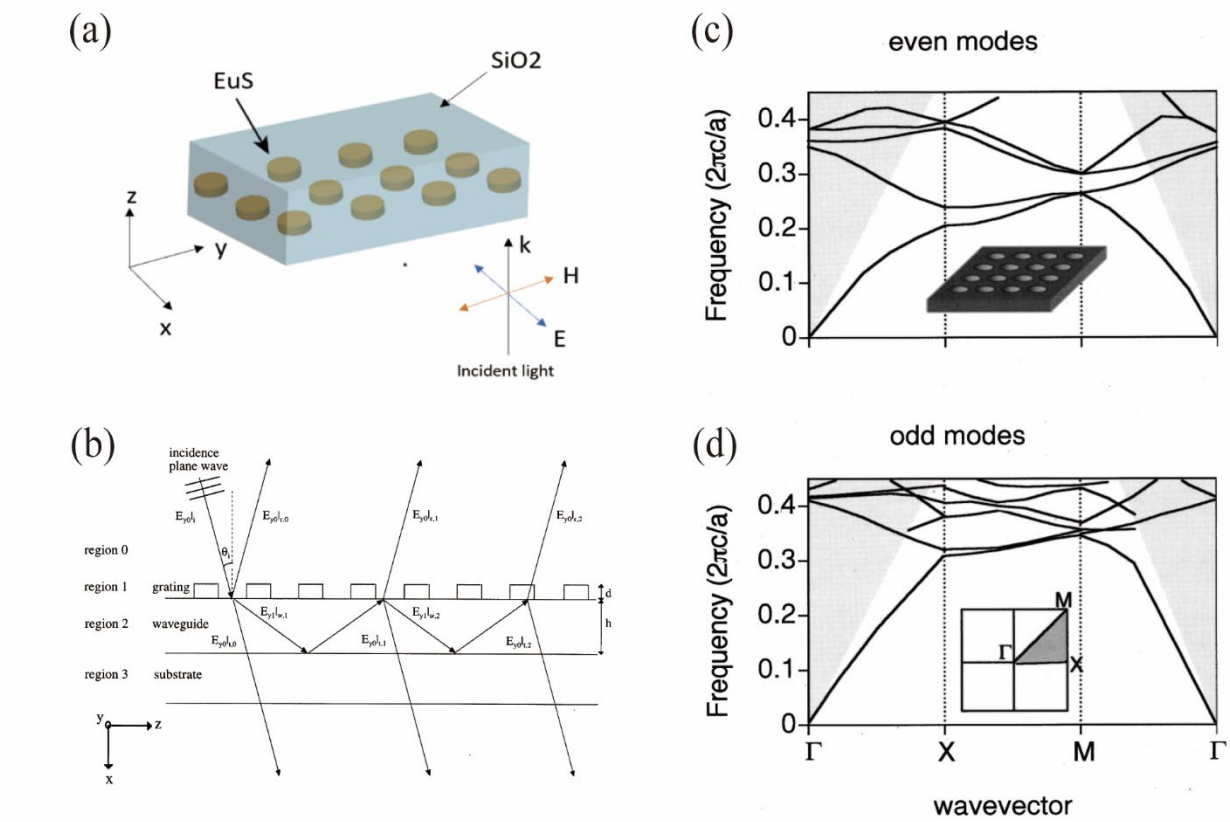

Fig. 7 Guided mode resonances (a) Schematics of the simulated structure of a EuS metasurface embedded in SiO2. (b) Principle of the guided mode resonance in a grating-waveguide structure with the ray optics picture. As a result of the interference between the partial waves reflected by the resonant grating the incident wave experiences high reflectivity at a certain wavelength and orientation angle. (c) Even and (d) odd mode band structure diagrams in a photonic crystal slab. The structure is shown in the inset of (c) and consists of a square lattice of air holes with the lattice constant **a** in a high-index dielectric slab. Even and odd modes are separated based on the field profile symmetry with respect to the mirror plane parallel to the slab. The gray region is the continuum of radiation modes above the light line. Solid lines outside the gray region are guided modes. Solid lines within the gray region are guided mode resonances.

4. 2 – Guided mode resonances in the EuS metasurface

As mentioned above, the designed metasurface is a 2-dimensional array composed of EuS pillars embedded in SiO2 matrix, as shown in Fig. 7 (a). This structure is also known as a photonic crystal (PhC) slab, which consists of a thin layer of material that has a periodic pattern of high and low refractive index regions. PhC slabs are well-known for supporting guided modes and guided mode resonances, which allow for various applications such as optical filters, waveguides, and sensors. The principle of guided mode resonances is shown in Fig. 7 (b) [A. Sharon, D. Rosenblatt, and A. A. Friesem, *JOSA A*, 14, 2985 (1997)]. The structure shown consists of a diffraction grating and a waveguide slab. The incident light is divided into three parts on the grating: directly reflected light, directly transmitted light, and diffracted light. Some of the diffraction orders match the waveguide modes of the structure, making the diffracted light confined in the waveguide. The confined light can be coupled out of the structure when it hits the grating again during each cycle. Therefore, the directly reflected/transmitted light and the light leaked from waveguide modes contribute to sharp resonant peaks/dips in the reflection/transmission spectrum, which is an important feature of guided mode resonances. The reflection and transmission of guided mode resonances can be modelled by the Fano resonance [U. Fano *Physical Review*, 124, 1866, (1961)], which describes the resonance effects where the transmission/reflection property is determined by the interference between direct and indirect light pathways. In the case of guided mode resonances, the transmitted amplitude *t* and the reflected amplitude *r* can be expressed as follows [Shanhui Fan and J. D. Joannopoulos *Physical Review B*, 65, 235112, (2002)]:

$$t = t_d + f\frac{\gamma}{i(\omega-\omega_0)+\gamma} \ , \tag{6}$$

$$r = r_d \pm f\frac{\gamma}{i(\omega-\omega_0)+\gamma} \ . \tag{7}$$

Here t_d and r_d are the direct transmission and reflection coefficients, ω_0 and γ are the center frequencies and widths of the Lorentzian from the resonance, and the factor f is the complex amplitude of the resonant mode. The plus and minus sign in Eq. (7) is determined by the field symmetry of the resonant mode. This model can give a good fitting to the line shapes of guided mode resonances.

Although a PhC slab lacks a distinct waveguide, its lattice structure can function as both a diffraction grating and a waveguide, so the same theory can be applied to PhC slabs. The waveguide modes in a PhC slab can be simply called guided modes, which are usually visualized by the band structure diagrams. An example is shown in Fig. 7(c)(d) [Shanhui Fan and J. D. Joannopoulos *Physical Review B*, 65, 235112, (2002)]. The two band structure diagrams describe the relationship between the frequency ω and the transverse wavevector component k_T of guided modes in a PhC slab consisting of a square lattice of air holes in a high-index dielectric matrix. The letters on the horizontal axis represent the three high-symmetry points in the Brillouin zone, as shown in the inset of Fig. 7 (d). This axis describes the wavevector path from Γ to X, to M, and back to Γ in the Brillouin zone. Additionally the are separated into guided modes into even and odd modes based on the field profile symmetry with respect to the mirror plane parallel to the slab. The even and odd modes are also known as TE (transverse electric) and TM (transverse magnetic) modes, respectively, based on the mirror reflection symmetry property of the electric and magnetic fields. It is also worth noting that the light line, which is defined as the boundary between the white region and the gray region, represent the ω-k_T relationship when the square of the *z* component of the wavevector k_z^2 equals to zero. Below the light line, k_z is an imaginary number since $k_z^2 < 0$, which indicates the field is evanescent in the *z* direction and the modes in the white region are protected inside the PhC slab without coupling out, while above the light line, k_z is an real number since $k_z^2 > 0$, which indicates the field is propagating in the *z* direction and the modes in the gray region are radiating out of the PhC slab. Therefore, the modes in the gray region show where guided mode resonances occur. In simulations or experiments, to demonstrate a guided mode resonance that is found from the band structure, one can set the frequency of the incident light as the frequency of the target mode and tune the incident angle of the light to make the incident k_T equal to the k_T of the target mode.

4.3 Parameter study of the EuS metasurface

Three geometrical parameters need to be determined in the parameter study: the lattice period a, the pillar radius R, and the pillar thickness L (see the inset of Fig. 8). Considering both the Verdet constant and absorption coefficient spectra of EuS [M.L. Meretska, et al. *Applied Physics Letters*, 120, 25 (2022)], we decided to do the study for the wavelength range between 700-800 nm, where EuS has both a relatively high Verdet constant and a relatively low absorption coefficient. For simplicity, normal incidence is used, and no absorption is considered in this simulation. Based on the guided mode resonance theory, we did a parameter sweep simulation with a reasonable parameter range and found two guided mode resonance dips in the transmission spectrum. When $a = 500\ nm, R = 230\ nm, L = 140\ nm$, the transmission spectrum is shown in Fig. 2. The left resonance dip with a sharp line shape indicates a high-Q resonance, while the right resonance dip with a broader linewidth indicates a relatively low-Q resonance. Both resonances exhibit residual transmittance.

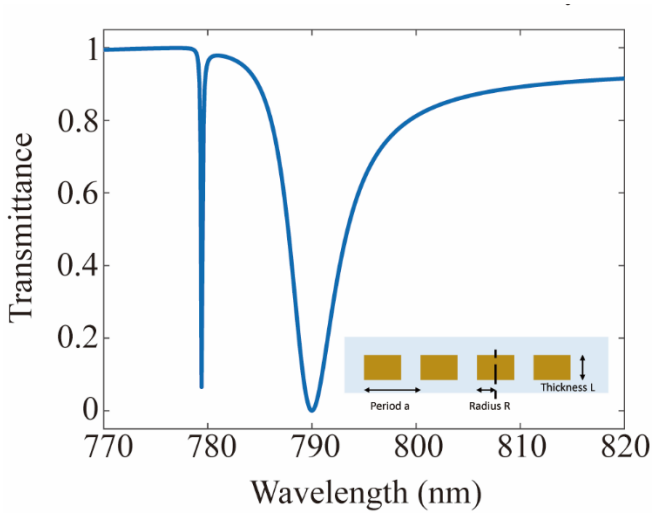

Fig. 8 – **Transmittance spectrum of the designed geometry in normal incidence**. The three geometrical parameters period a=500 nm, pillar radius R=230 nm, and pillar thickness L=140 nm. No material absorption is assumed. A high-Q resonance and a low-Q resonance are found in the wavelength range between 700-800 nm. The inset shows a side view of the structure and the three geometrical parameters.

To further characterize these two resonances, we conducted two additional parameter sweep simulations. First, we examined how the spectral positions of the high-Q and low-Q resonances vary with changes in the lattice periods in the x and y directions (a_x and a_y), while maintaining other parameters constant. The findings are presented in Fig. 3. In Fig. 9 (a), we vary a_x while preserving $a_y = 500\ nm$. The low-Q resonance's spectral position, marked by the white dashed line, remains almost constant. However, the high-Q resonance's spectral position, marked by the red dashed line, significantly depends on a_x. As a contrast, in Fig. 0 (b), we observe that the low-Q resonance's spectral position shifts with changes in a_y, but the high-Q resonance's position remains largely unaffected. These results show that the high-Q and low-Q resonances are exclusively related to the x and y directions, respectively, suggesting the directionality of their underlying guided modes.

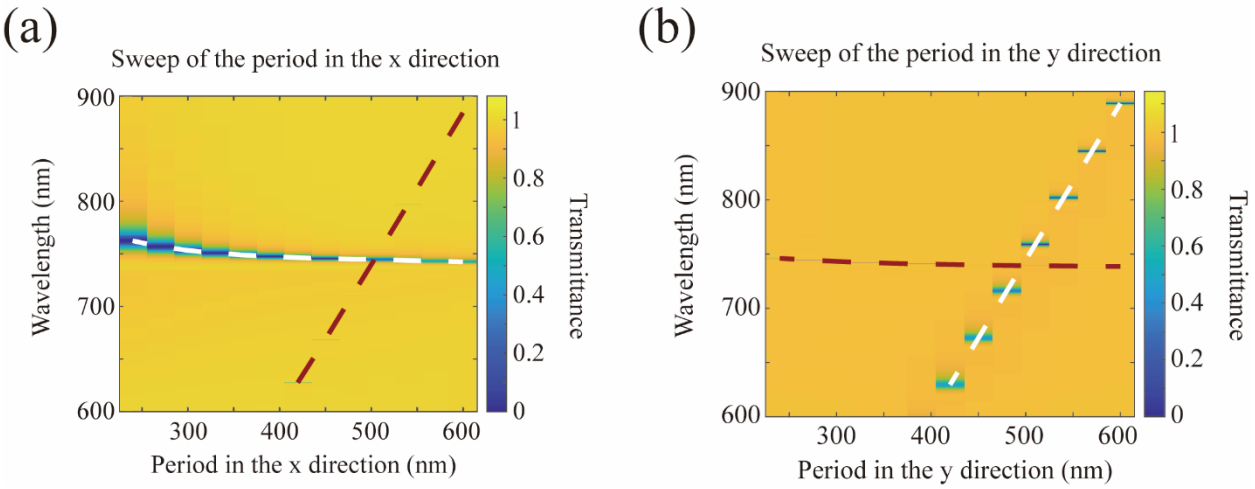

Fig 9 Transmittance spectra map for varying lattice periodicity in the x and y directions. (a) The change of the period in the x direction causes the high-Q resonance to spectrally shift. (b) The change of the period in the y direction causes the low-Q resonance to spectrally shift. The dashed lines in (a) and (b) trace the positions of the two resonances, where the low-Q resonance is outlined with the white dashed line and the high-Q resonance is traced with the red dashed line.

The second simulation is to examine the responses of the resonances to small changes in the incidence angle. In this simulation, all the geometrical parameters are kept constant, and the incident plane is fixed as the *x*-*z* plane, which means that the incident transverse wavevector k_T is along the *x* direction. We set the incident polarization as s-polarization (polarization perpendicular to the incidence plane) or p-polarization (polarization parallel to the incidence plane) and sampled a few small incidence angles from 0.2 to 1.2 degrees. Some results are shown in Fig. 10. In the case of normal incidence, as shown in Fig. 8, we observe one high-Q resonance and one low-Q resonance. However, when the incidence angle is non-zero, resonance splitting occurs. Specifically, for p-polarization incidence, the high-Q resonance is split into two, while the low-Q resonance at the wavelength of 755 nm is unaffected (see Fig. 10 (a)(b)). As a contrast, for s-polarization incidence, the low-Q resonance is split into two, while the high-Q resonance around the wavelength of 755 nm is almost unchanged (see Fig. 10 (c)(d)). In addition, when the incidence angle increases, the split resonances shift farther apart from each other for both polarization situations. The resonance splitting indicates that both the high-Q and low-Q resonances might correlate with doubly degenerate guided modes, and that these modes are sensitive to small-angle oblique incidence with particular polarizations.

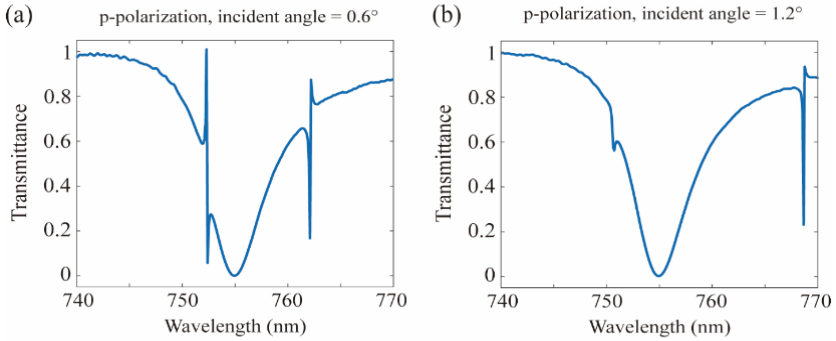

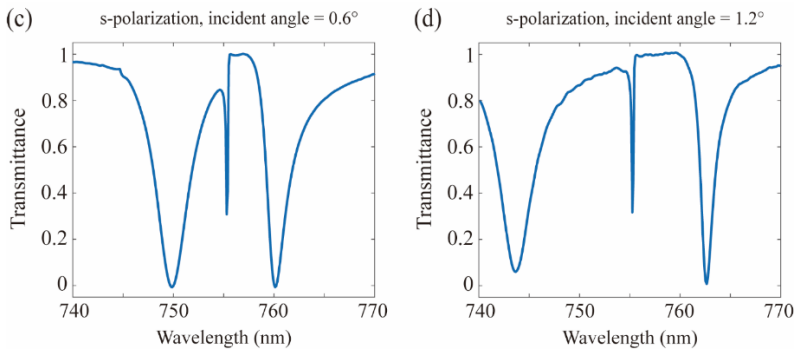

Fig. 10 – Transmittance spectra with small-angle oblique incidence and s- or p- polarization. The simulation setting for the subfigures: (a) p-polarized incident light, incidence angle= 0.6 deg; (b) p-polarized incident light, incidence angle = 1.2deg ; (c) s-polarized incident light, incidence angle= 0.6 deg; (d) s-polarized incident light, incidence angle= 1.2 deg. When incident angle is not zero, the high-Q resonance is split into two if the incident light is p-polarized, while the low-Q resonance is split into two if the incident light is s-polarized. The larger the incidence angle is, the farther the split resonances shift apart from each other.

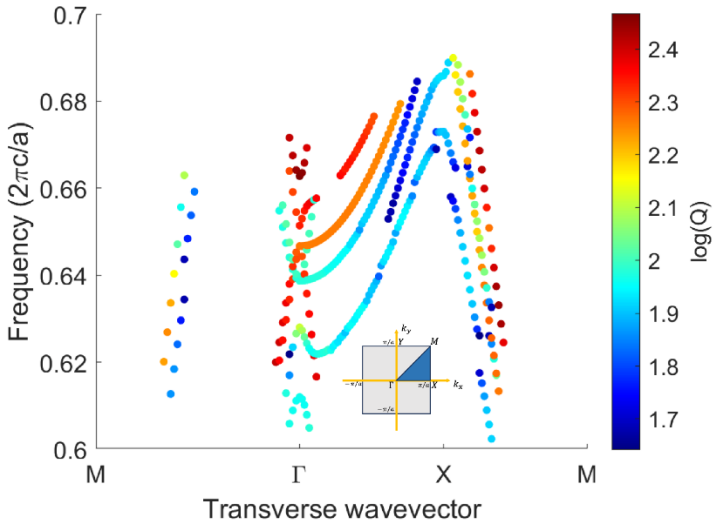

Fig. 10 Band structure of the designed metasurface in the frequency region of interest. The frequency in the y axis is normalized by the factor 2πc/a, where c is the speed of light and a is the lattice constant. The color of each sample point marks the log value of its Q factor. The inset shows the Brillouin zone of the designed structure.

4.5 – Mode analysis based on the band structure

To better understand the nature of the high-Q and low-Q resonances, we calculated the band structure of the designed device to look for the guided modes related to the two resonances. We set the geometrical parameters $a = 500\ nm, R = 230\ nm, L = 140\ nm$ (the same setting as in Fig. 8) and searched for modes around the wavelength of 785 nm. The calculated band structure diagram is shown in Fig. 10. Same as in Fig. 7 (c)(d), the horizontal -axis is the path of the transverse wavevector k_T in the Brillouin zone (see the inset of Fig. 10), and the *y*-axis is the mode frequency normalized by $2\pi c/a$. The color of each sample point marks its Q factor. Fig. 10 shows that there are many bands in this region, which makes it hard to identify the modes related to the resonances we observed. For clarity, we only keep the k_T range from Γ to X ($k_T = k_x$ in this case) and divide all the modes into TE and TM modes, as shown in Fig. 11 (a)(b). Based on the results in Fig. 11, we identify the two modes circled along the *y* axis in the TE mode and TM mode

diagrams as the guided modes related to the low-Q and high-Q resonances, respectively, for at least three reasons. First, the frequencies of the TE and TM modes match the wavelengths of the low-Q and high-Q resonances in Fig. 8. It also makes sense that the TE mode has a smaller Q factor than the TM mode as marked by the color in Fig. 11(a)(b). Second, both the circled TE and TM modes are doubly degenerate modes when $k_x = 0$, and increasing k_x breaks the degeneracy. This corresponds to the observation of resonance splitting when the incident angle is not zero. Fig. 11 (c)(d) and (e)(f) show the H_z and E_z field profiles of the doubly degenerate TE and TM modes when $k_x = 0$, respectively. We can find that the double degeneracy is generated because of the two possible polarization of the fields. To understand why the high-Q and low-Q resonances are exclusively sensitive to the p-polarized and s-polarized light, respectively, one needs to understand the relationship between the incident polarization and the excited mode type. Consider normal incident light with p-polarization in the *x*-*z* plane. When it is diffracted by the PhC slab and coupled into guided modes, the polarization has to be preserved. Specifically, since the incident light has the E field in the *x* direction and H field in the *y* direction, the diffracted light propagating in the *x* direction still has its H field in the *y* direction, resulting in a TM mode, while the diffracted light propagating in the *y* direction still has its E field in the *x* direction, resulting in a TE mode. Therefore, when p-polarized light has a non-zero incident angle in the *x*-*z* plane, it gives a non-zero k_x to TM modes, leading to the degeneracy breaking of the circled TM mode and splitting of the high-Q resonance. In contrast, when s-polarized light has the same incidence angle, it will give a non-zero k_x to TE modes, leading to the degeneracy breaking of the circled TE mode and splitting of the low-Q resonance. Third, with the discussion above, we know that TE modes are polariazed in the *y* direction while TM modes arepolarized in the *x* direction for normal incidenc. Since we observed that the spectral positions of the high-Q and low-Q resonances depend exclusively on the period in the *x* direction and *y* direction, respectively, we know that the high-Q and low-Q resonances are related to a TM mode and a TE mode, respectively. *In conclusion for the parameter study and band structure analysis, the high-Q resonance is related to a doubly degenerate TM guided mode, while the low-Q resonance is related to a doubly degenerate TE guided mode.*

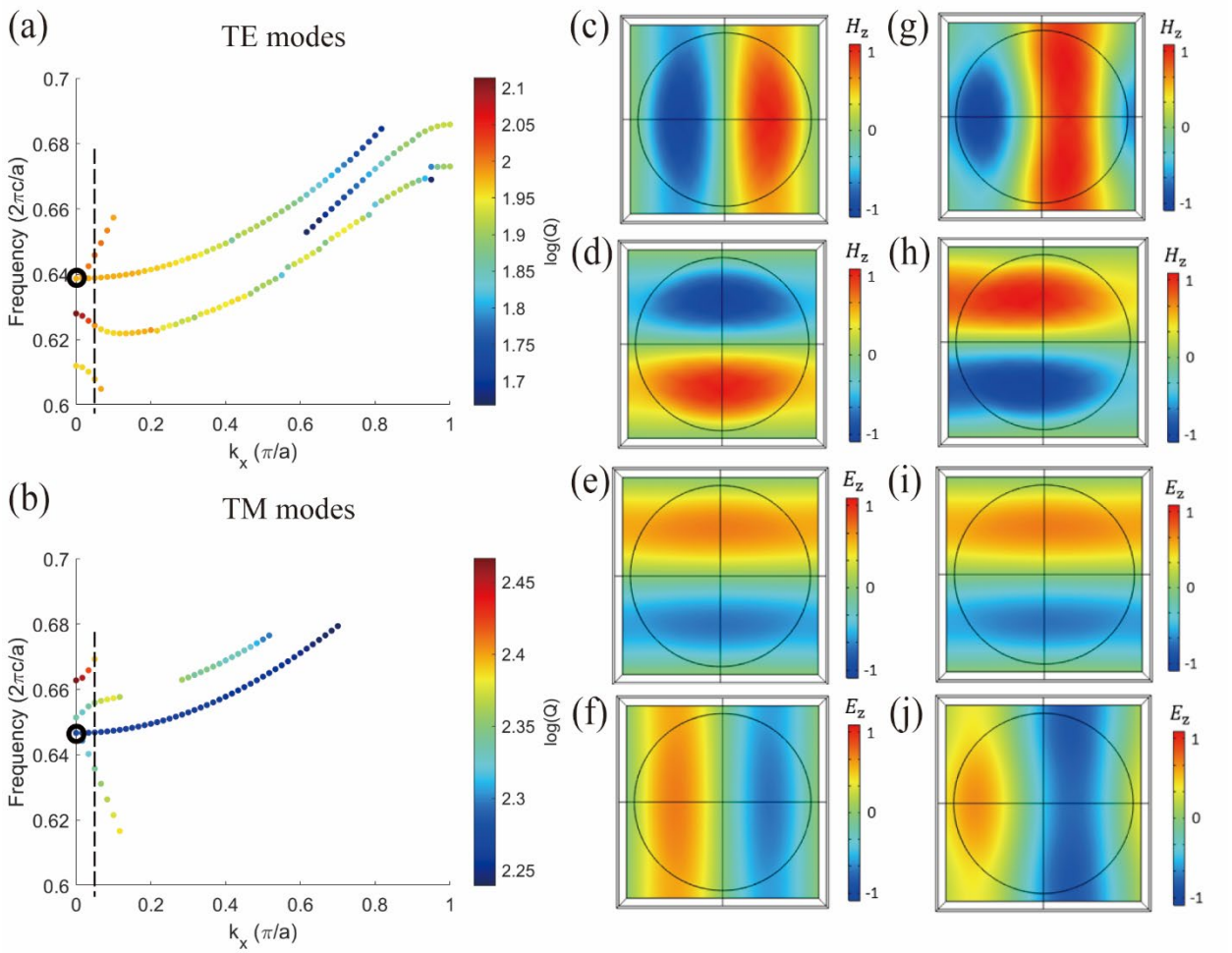

Fig. 11 – Band structure for TE (a) and TM (b) modes with the transverse wavevector from Γ to X (i.e. k_x from 0 to π/a, where a is the lattice constant) and 8 field profiles in the x-y plane. Specifically, (c) and (d) are two H_z field profiles for the doubly degenerate mode circled on the y axis in (a); (e) and (f) are two E_z field profiles for the doubly degenerate mode circled on the y axis in (b); (g) and (h) are the evolved field profiles from (c) and (d) when normalized $k_x = 0.05$, as indicated by the dashed line in (a); (i) and (j) are the evolved field profiles from (e) and (f) when normalized $k_x = 0.05$, as indicated by the dashed line in (b). These results reveal that the low-Q and high-Q resonances correspond to the doubly degenerate modes circled in (a) and (b), respectively.

4..6 – Design of a high-performance metasurface-based Faraday rotator

The resonances discussed above have the ability to produce large Faraday rotation, but show very low transmittance, as shown in Fig. 8,9,10. The reflectivity is correspondingly high but for a practical device one wourl want to achieve high transmission. We have shown that by overlapping the spectral positions of the TE and TM guided mode resonances to generate a four-fold degenerate state, high transmittance can be achieved. As shown in Fig. 12(a), we sweep the pillar radius R while keeping $a = 500\,nm$, $L = 140\,nm$, and the resonance overlapping condition is found when $R = 165\,nm$, marked by the left dashed line. Fig. 12 (b) shows the transmittance spectrum plot for this pillar radius. A near-100% transmission is achieved at the wavelength of around 755 nm, where the two resonances overlap. Note that this simulation was performed without accounting for material absorption, as it allows for precise identification of the resonances.

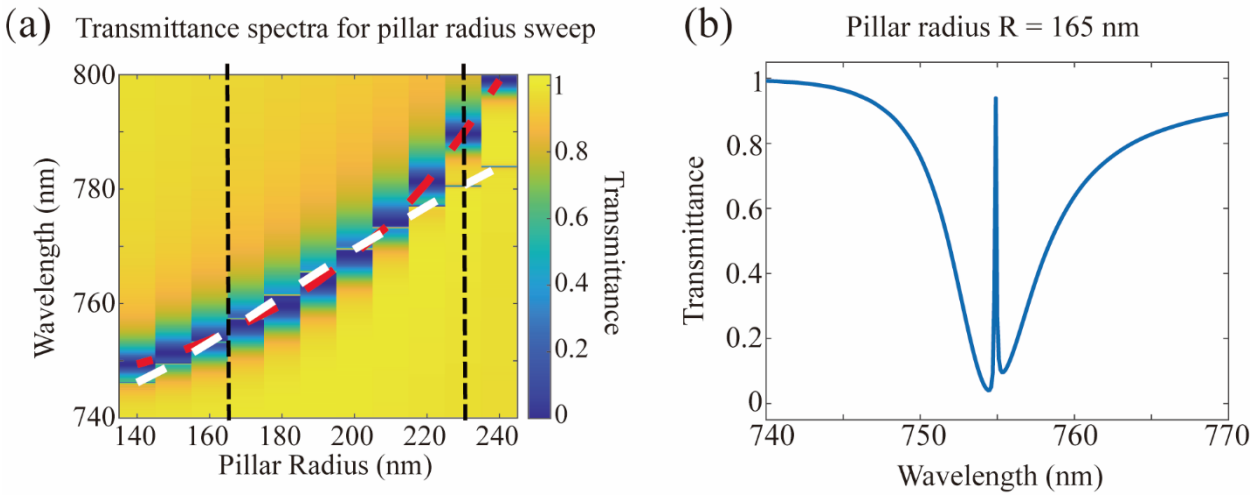

Fig, 12 – The transmittance spectra for the high-performance design. (a) The transmittance spectra map for different EuS pillar radii with the fixed parameters of the lattice constant a = 500 nm and the pillar thickness L = 140 nm. The dashed red and white lines trace the positions of the TE guided mode resonance (low-Q) and TM guided mode resonance (high-Q), respectively. (b) The transmittance spectrum when the two resonances spectrally overlap, corresponding to the left dashed line in (a). The transmittance at the resonance overlap is near 100%. The right dashed line in (a) corresponds to the spectrum in Fig. 2.

To evaluate the enhancement of the Faraday effect in this EuS metasurface, we performed simulations of the Faraday rotation angle for the two pillar radii that correspond to the overlapping and spectrally separated resonances (see Fig. 12 (b) and Fig. 7). We observe the enhancement of the Faraday effect at the spectral positions of the TE and TM guided mode resonances in the spectrally separated resonance condition, as shown in Fig. 13 (b). This is the expected result, and it demonstrates the validity of the simulation model that we used. Furthermore, the highest absolute value of the Faraday rotation is achieved at the position of the TM guided mode resonance and is equal to ~0.05 deg.

In the overlapping resonance condition, we observe an enhancement of the Faraday effect at the position of the resonance overlap, and the Faraday rotation angle is equal to ~0.18 deg, as shown in Fig. 13 (a). We observe a 3.6 times improvement compared to the spectrally separated resonance condition. Although the enhancement of the Faraday effect is clearly visible, we need to consider the transmittance of the structure at the given wavelength. It can be done by introducing the figure of merit (FOM) that is commonly used to evaluate the performance of the Faraday effect [A. B. Khanikaev, A. V. Baryshev, A. A. Fedyanin, A. B. Granovsky, and M. Inoue *Optics Express*, 15, 6612 (2007)]:

$$FOM = \sqrt{T}|\theta|. \quad (8)$$

Here T is the transmittance, and θ is the Faraday rotation angle. We plot the FOM as a function of the wavelength for the selected pillar radii (see Fig. 13 (c)(d)). The highest FOM value for the overlapping resonance condition is ~0.17, which is 5.3 times higher than the highest FOM for the spectrally separated resonance condition. In addition, we evaluated the performance of our device against a uniform EuS layer with the same thickness. The FOM value for our design is ~ 24 times higher than a thin film, demonstrating a clear superiority of the proposed geometry.

In conclusion for this section, we simulated the EuS metasurface design and achieved high transmission, large Faraday rotation, and large FOM in the condition when the TE and TM guided mode resonances spectrally overlap. This approach is more promising and practical than the Kerker condition [M. Decker, et

al. *Advanced Optical Materials*, 3, 813, 2015], which instead utilizes the resonances in each individual meta-atom.

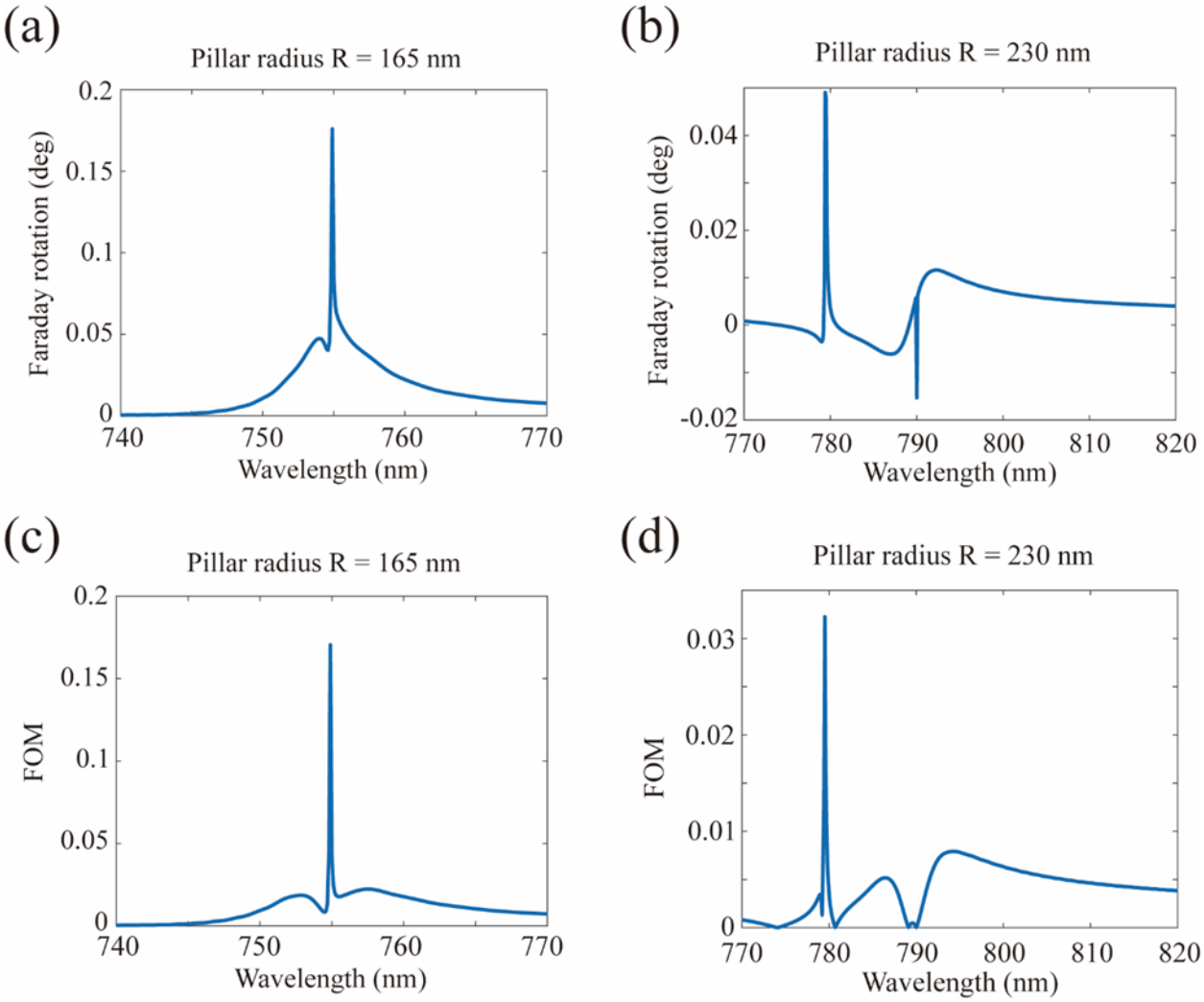

Fig. 13 – Faraday rotation angle and figure of merit (FOM) for the TE and TM guided mode resonances. (a) The Faraday rotation angle as a function of wavelength in the overlapping resonance condition. (b) The Faraday rotation angle as a function of wavelength in the spectrally separated resonance condition. (c) FOM as a function of wavelength in the overlapping resonance condition. (d) FOM as a function of wavelength in the spectrally separated resonance condition. In the overlapping resonance condition, a high Faraday rotation angle and a high FOM value are obtained at the wavelength of resonance overlapping (~755 nm), suggesting high performance of our designed device at this wavelength.

4.7 – Fabrication of EuS metasurfaces

As the new EuS deposited by our MIT collaborators, Y. Hou and Prof. J. Moodera, no longer dissolves in solvents, we updated the fabrication protocol to a lift-off process (see Fig. 14), which is simpler and more efficient than the fabrication processes presented in the previous reports. The new process only consists of four steps: electron-beam lithography writing on ZEP resist, EuS deposition by our collaborators, ZEP resist removal with remover PG, and SiO_2 deposition to embed the EuS pillars.

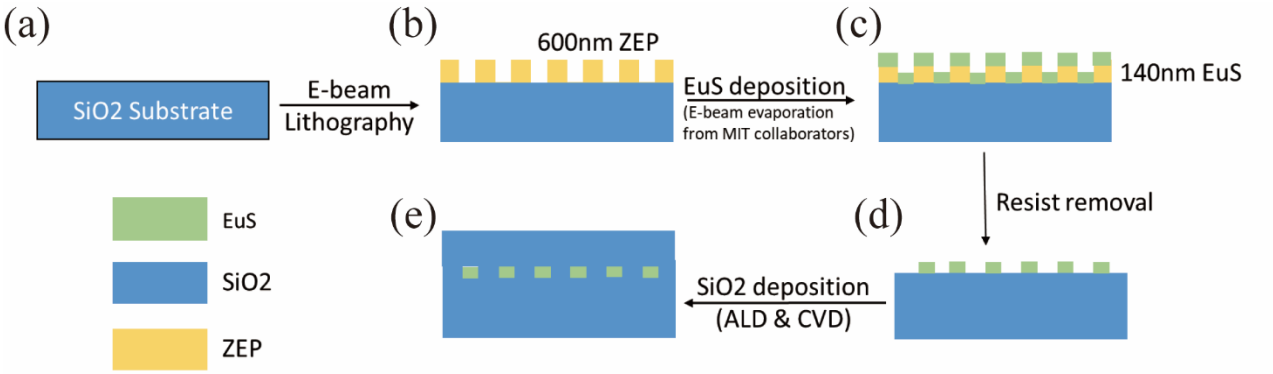

Fig. 14 – The workflow of the fabrication process. The acronyms in the parentheses refer to the fabrication tools. ALD, atomic layer deposition; CVD, chemical vapor deposition.

Fig. 15 (a) and (b) present a zoom-out and zoom-in view of the fabricated sample cross section at stage (e), respectively. Although the tilted sidewalls of the EuS pillars are an unsolved issue for all the fabrication protocols we have tried, the dimensional measurements of this new sample reveal that the lattice period, pillar thickness, and pillar radius well match our design, making these samples promising for the optical measurement. The sidewall angle of the EuS pillars in this device is ~65 degrees.

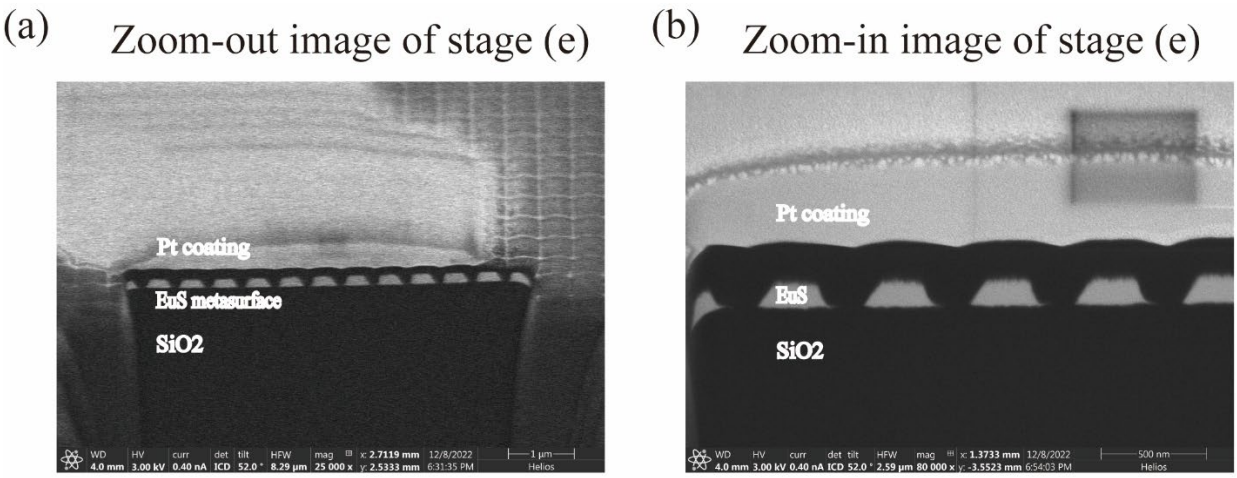

Fig. 15 Focused ion beam microscopy (FIB) images of the sample fabricated with the workflow in Fig. 14. (a) and (b) are a zoom-out image and a zoom-in image of the stage (e) of the fabrication process. The dimensions of the three geometrical parameters well match our design, and the only problem is the tilted sidewalls of the EuS pillars.

4.8 – Robustness study

Before doing optical measurement, we studied the robustness of the designed metasurface against the tilted sidewall geometry that occurs during the fabrication described above. Setting $a = 500\,nm, R = 145\,nm, L = 140\,nm$, and a sidewall angle of 65 deg, we calculated the transmission spectrum, Faraday rotation angle, and FOM for the design with tilted sidewall pillars. Material absorption is also considered in this simulation. The results are presented in Fig. 16. While the design with straight pillar sidewalls and zero absorption can reach near-100% transmittance in the overlapping resonance condition (Fig. 12 (b)), this design, which is closer to the real fabricated devices, possesses ~33% transmittance in the same condition.

In Fig. 16 (b)(c), this device possesses a maximum Faraday rotation angle of ~0.09 deg and a maximum FOM value of ~0.025, which are ~11.3 and ~3.1 times larger than their counterparts in the same-thickness uniform EuS film.

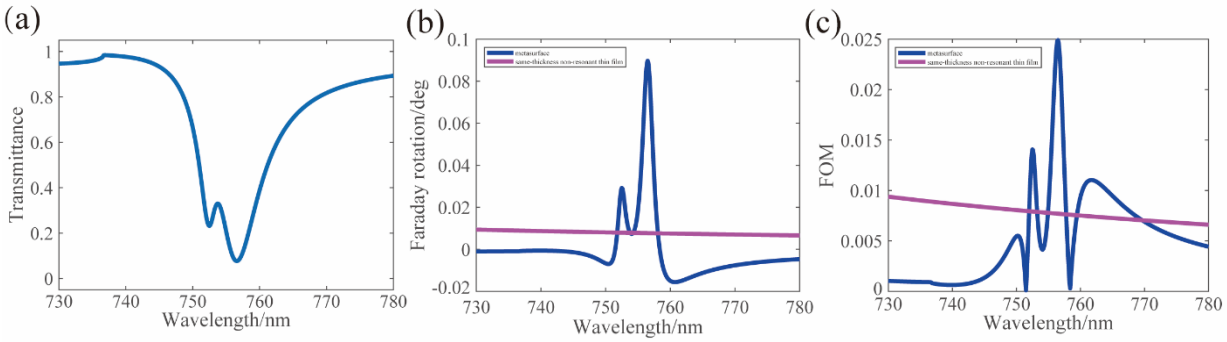

Fig. 16 – Transmittance (a), Faraday rotation (b), and FOM (c) of a structure with a tilted sidewall angle. Parameter setting: a=500 nm, R=145 nm, L=140 nm, sidewall angle=65 deg. Normal incidence is applied, and material absorption is considered. Compared to the structure with straight pillar sidewalls, the transmittance at the wavelength of resonance overlapping drops from ~100% to ~33% for the tilted pillar sidewall design. Nevertheless, its maximum FOM is still ~3.1 times larger than the same-thickness uniform EuS film, suggesting it is still worth doing the optical measurement.

4.9 – Transmittance measurements

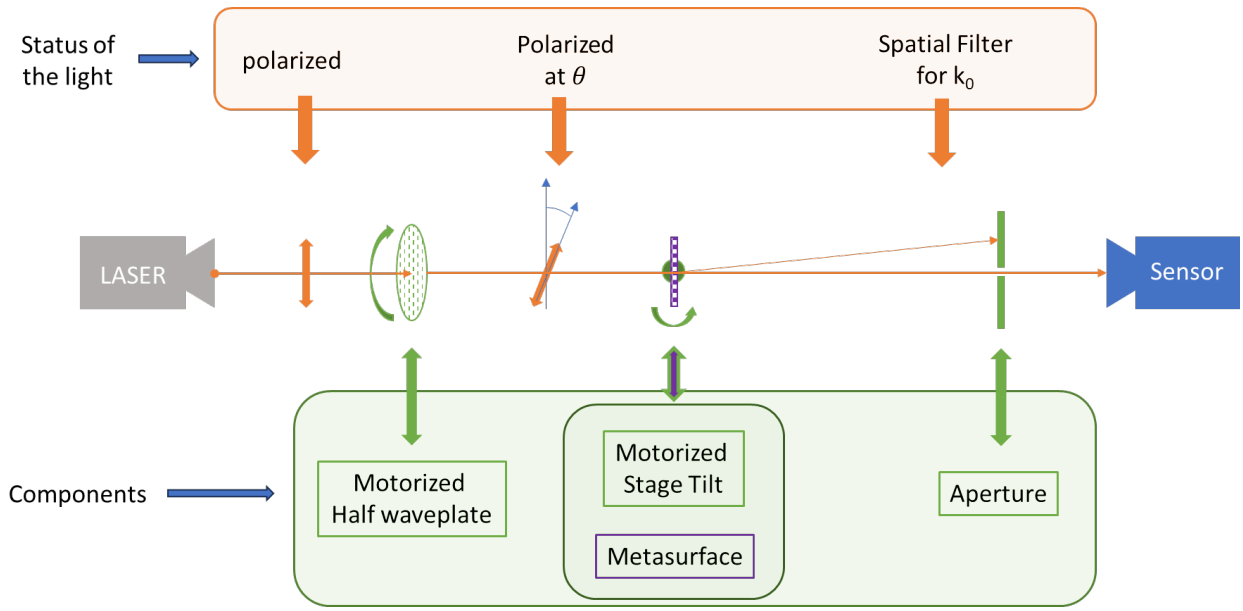

Fig. 17. Set-up for the transmittance measurement. The laser output passes through a polarizer, a half waveplate, the sample, and an aperture, and is finally collected by the sensor. This set-up has the ability to precisely change the wavelength, polarization, incident angle of the light, making it suitable for the guided mode resonance measurement.

The transmittance measurement set-up is shown in Fig. 17. The laser output passes through a polarizer, a half waveplate, the sample, and an aperture, and is finally collected by the sensor. This set-up allows for the control of multiple degrees of freedom, such as wavelength, polarization, incidence angle, etc. The stage tilt and half waveplate are controlled precisely by the motors to overcome the high sensitivity of the guided mode resonances to the incidence angle and polarization.

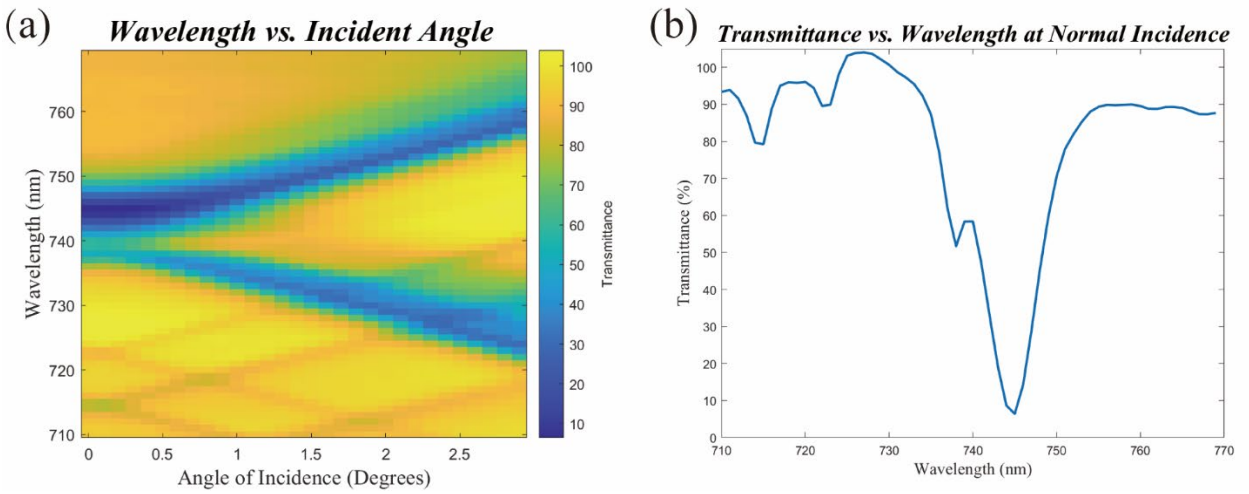

Fig. 18 –Transmittance spectra measurement. (a) The transmittance spectra map as a function of the wavelength and incident angle. It can be clearly seen that the resonances are splitting when the incident angle increases. (b) The transmittance spectrum plot when the incident angle is zero. The two resonances between the wavelength 730 nm and 755 nm and the overlapping resonance condition are our expected results and match the simulation in Fig. 11 (a) very well.

The measured transmittance spectra map as a function of the wavelength and incident angle is presented in Fig. 18 (a) for a sample with a=500 nm, R=145 nm, L=140 nm. When the incidence angle is zero, the transmittance spectrum is plotted in Fig. 18 (b). In the wavelength range between 730-755 nm, the spectrum shows two resonances and the overlapping resonance condition and matches the simulation in Fig. 16 (a) very well. When the incidence angle increases, both resonances split (see Fig. 18 (a)). Since the incident light of this measurement has both p- and s-polarizations, it makes sense that both the TE and TM guided mode resonances are affected and experience splitting when the incidence angle is not zero.

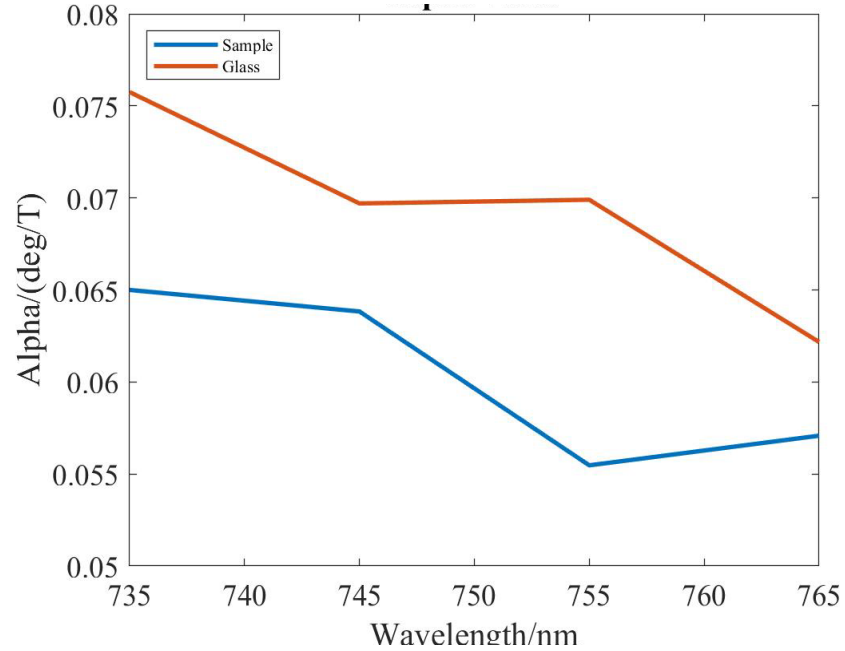

Fig.19– Alpha value spectra measurement. The alpha value α is used to characterize the strength of the Faraday effect. This figure shows the alpha value spectra of the sample and a bare glass substrate. The alpha values of the sample are always smaller than the glass substrate because the Verdet constants of glass and EuS have opposite signs.

4.10 – Faraday rotation measurements

The measurement set-up and method are presented in detail in our previous publication [M. Mereszka et al. *Applied Physics Letters* 120, 25, 2022] on this project. To characterize the strength of the Faraday effect, the alpha value α is introduced and is defined as

$$\alpha = \frac{\theta_{PR}}{B} \ . \tag{9}$$

Here θ_{PR} is the polarization rotation angle, and B is the magnetic field applied to the sample.

For each wavelength, we sampled a few different magnitudes of the magnetic field B and measure their corresponding Faraday rotation angles θ_{PR}. The alpha value α is obtained by linearly fitting θ_{PR} and B. Preliminary alpha value spectra of the sample and a bare glass substrate are plotted in Fig. 19. Note that the Verdet constants of glass and EuS have opposite signs [M. Mereszka et al. *Applied Physics Letters* 120, 25, 2022]. Therefore, their Faraday rotations are intrinsically in the opposite directions, and their alpha values also have opposite signs, which explains why the alpha value of the sample is smaller than the alpha value of the glass substrate in Fig. 19. To compare with the Verdet constants of bulk materials, we can define the "effective" Verdet constant of our EuS metasurface as

$$V_{eff} = \frac{\alpha_{metasurface}}{L_{metasurface}} \ . \tag{10}$$

Here $\alpha_{metasurface}$ is the alpha value of the metasurface layer without the substrate, and $L_{metasurface}$ is the thickness of the metasurface. Taking the wavelength 755 nm as an example, $\alpha_{metasurface} = \alpha_{sample} - \alpha_{substrate} = -0.0144\ deg/T$, and $L_{metasurface} = 155\ nm$, so we get $V_{eff} = -9.31 \times 10^4\ deg/(T * m)$. This value is ~2 times larger than the Verdet constant of bulk EuS at the same wavelength, which is around $-5 \times 10^4\ deg/(T * m)$.

In conclusion we successfully observed the high-Q and low-Q resonances and the overlapping resonance condition in the transmittance spectrum measurement. We also got a ~2 times Faraday rotation enhancement with our sample. An optimization of the Faraday rotation measurement set-up is needed to obtain more reliable results with high signal-to-noise ratios.

5. Compact integrated non-reciprocal devices

The opto-isolator based on Faraday rotation is the prototypical nonreciprocal device. This has led us to consider new mechanisms to achieve optical non reciprocity. In the course of this work, we have invented and realized a new class of optical resonators where the propagation of light is asymmetric. To achieve that mirrors are designed in such a way that the back reflected light propagates in a resonator mode different that the forward propagating light. This cascaded mode conversion leads to radically different behavior compared to standard resonators such as Fabry-Perot.

5.1 Cascade-mode conversion optical resonators

In this section we present recent work on a new resonator concept that can lay the ground to novel norn-reciprocal devices. The functionality of electromagnetic resonators can be understood from the constructive interference of waves—creating resonant modes. A crucial parameter that determines these modes is the round- trip phase $\Delta\phi$, accumulated by the field after completing one round trip in the resonator[2]. Waves that pick up a round-trip phase equal to a multiple of 2π constructively interfere with themselves and become

resonant modes of the resonator (Fig. 20a). In the case of a Fabry-Perot geometry, the resonance condition is then given by

$$2Ln\frac{2\pi\nu}{c} + 2\phi_r = 2\pi m, \tag{11}$$

where ν is the frequency of light, m is an integer number representing the index of the resonant modes of frequency ν_m, c is the speed of light in vacuum, L is the length of the resonator, n is the refractive index of the material inside the resonator, and ϕ_r is the reflection phase at the mirrors. This simple equation explains two essential properties of resonators: the existence of the fundamental mode and the appearance of a spectrum with only a discrete number of modes. The resulting frequency spectrum from Eq. (6) is then given by $\nu_m = c(m - \phi_r/\pi)/(2nL)$. Above, we ignore the properties of the mode in the transversal plane. Typically, a discrete number of orthogonal transverse modes exist for each frequency, e.g., TE_i and TM_i waves, where each transverse mode experiences a different effective index ($n_{eff,i}$). As a result, the resonant modes of a resonator generally consist of a superposition of spectra, corresponding to the various families of transverse modes (Fig. 20b). The spectra are given by:

$$\nu_{i,m} = \frac{c(m - \phi_{r,i}/\pi)}{2n_{\mathrm{eff},i}L}. \tag{12}$$

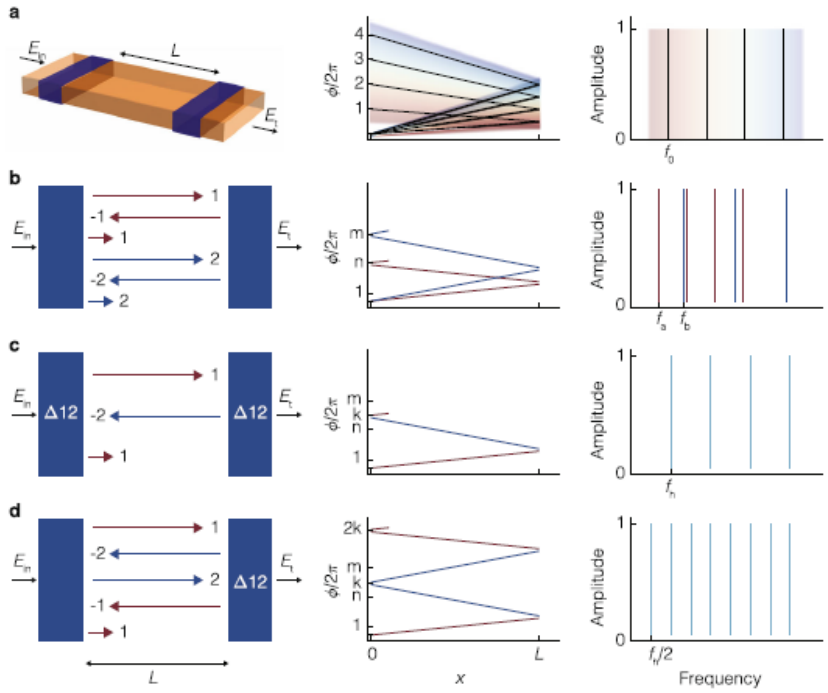

Fig. 20 The operating principle underlying cascaded-mode resonances. **a** From left to right: First, **a** visualization of traditional resonator of length L. Second, the phase shift as a function of distance x for a resonator of length L for different longitudinal modes of index m after a round trip 2L the accumulated phase is m2π. Third, the resonance spectrum, which corresponds to the frequencies for which the round-trip phase Δϕ equals a multiple of 2π. **b** In many resonators, different transverse modes contribute to different spectra because their effective refractive indices inside the resonator differ. The different effective indices determine the different slopes of the lines in the second column, which results in spectra with different fundamental modes (f_a, f_b) and mode spacings in the third column. **c** A cascaded-mode resonator (the blue regions are mode-converting mirrors) in which the two transverse modes, labeled 1 and 2, couple into one supermode, with

fundamental frequency f_h. The round-trip phase and the free spectral range are partly determined by the effective indices of mode 1 (red slope) and of mode 2 (blue slope). d A cascaded-mode resonator in which a supermode is created where both mode 1 and mode 2 circulate twice through the resonator before completing the round trip. There is one spectrum, with fundamental mode and free spectral range halved compared to c. The labels in the resonators in the first column refer to the mode conversions that take place in the blue regions: Δ_{12} implies that mode 1 is reflected into mode 2, and vice versa. Blue regions without label refer to traditional mirrors where each mode is reflected into itself.

We now introduce a new type of resonator based on cascaded mode coupling. This coupling is implemented by mode-converting mirrors that not only reflect incident waves, but also simultaneously convert them to another transverse mode profile. We illustrate this principle in Fig. 20c, d: upon reflection on the rightmost mode converting mirror, an incident wave with a particular transverse mode profile is converted into another transverse mode. When this mode returns to the leftmost mirror, another mode conversion occurs upon reflection. This non-reciprocal propagation consisting of cascade of mode conversions can be repeated as many times as the number of transverse modes supported by the waveguide. Finally, a "supermode" emerges when the wave is converted back to the original configuration of the incident mode. For resonators with N different transverse modes, the round-trip phase is given by:

$$\Delta\phi = k_0 L \xi \sum_{i=1}^{N} n_{\mathrm{eff},i} + \phi_{r,\mathrm{tot}}. \qquad (13)$$

Here k_0 equals $2\pi/\lambda_0$ with λ_0 the vacuum wavelength, $\phi_{r,\mathrm{tot}}$ is the sum of all reflection phases, and ξ is the parameter that encodes whether the contributing transverse modes appear once ($\xi = 1$) or twice ($\xi=2$) in the chain. The round-trip phase is thus no longer merely determined by the length of the resonator and the refractive index but also by the number of coupled transverse modes. The corresponding resonance condition is

$$\nu_m = \frac{c\left[m - \phi_{r,\mathrm{tot}}/(2\pi)\right]}{L\xi \sum_{i=1}^{N} n_{\mathrm{eff},i}}. \qquad (14)$$

The free spectral range is thus set by the denominator which represents the sum of the round-trip optical paths of the different cascaded modes $L\xi \sum_{i=1}^{N} n_{\mathrm{eff},i}$ rather by $2n_{\mathrm{eff},i}L$ as in a conventional resonator. Next, whereas traditional resonators feature an incoherent superposition of different spectra, each corresponding to a different transverse mode, cascaded-mode resonators exhibit just one superspectrum (Fig. 20 c, d). This analysis is independent of how the mode conversions are realized. For instance, in the context of transverse modes in waveguides, a mode converter can be implemented using a specific refractive index variation (blue regions in Fig. 20 a–d).

An interesting feature of cascaded-mode resonances, in agreement with the geometrical model described above, is the modification of the free spectral range $\Delta\nu$, given by:

$$\Delta\nu = \frac{c}{\xi \sum_{i=1}^{N} n_{g,i} L}, \qquad (15)$$

where $n_{g,i}$ is the group index of transverse mode i at frequency ν.

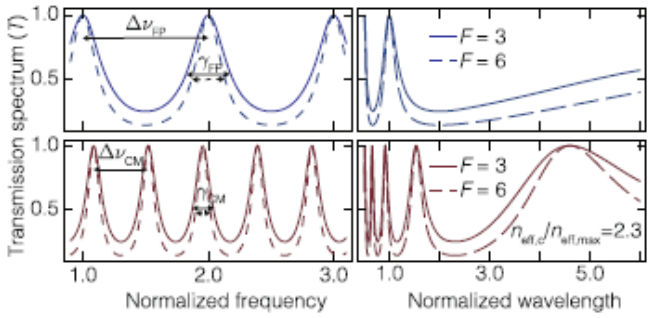

Fig 21 The spectral properties of cascaded-mode resonances. The spectra of a traditional resonator compared with the spectra of a cascaded-mode resonator versus frequency (left) or wavelength (right). The blue and red spectra respectively correspond to conventional resonators and cascaded-mode resonators with $n_{eff,c}=n_{eff,max}=2.3, \phi_{r,tot}=1.5\pi$. The solid and dashed lines correspond to a resonator's finesse equal to 3 and 6, respectively. Note the reduction of the free spectral range Δν and linewidth γ when several transverse modes are coupled.

Two other crucial spectral parameters can be engineered in a cascaded mode resonator by controlling the round-trip phase: the linewidth γ and the quality factor Q (Fig. 21). Unlike the free spectral range, the linewidth and the quality factor depend on the round-trip losses. Not only the spectral properties but also the temporal and spatial properties of these modes can be engineered by using cascaded-mode coupling. The intracavity power build-up and the intracavity power build-up time both scale proportionally to the number of coupled modes. While the intensity of longitudinal modes in traditional resonators exhibits a simple standing-wave profile, the intensity profile in a cascaded-mode resonator will have a more irregular profile, potentially with many different local minima and maxima.

A unique spatial property of cascaded-mode resonators is that the propagation constant of a supermode depends on the propagation direction. This phenomenon is shown in its most straightforward implementation in Fig. 20c. When a field with transverse profile of mode 1 is incident on the left side of this resonator, a cascaded mode will exist with wave vector $k = k_{0neff,1}$ propagating from left to right, and a wave vector $k = k_{0neff,2}$ propagating from right to left. Due to the distinct propagation constants in opposite directions, directional nonlinear optical effects can occur in the resonator since the phase matching conditions may only be satisfied in one direction. The directionality could also give additional control over chiral, optomechanical, or quantum mechanical interactions inside the resonator. A final property of cascaded-mode resonances that deserves special attention is the existence of mode-independent spectra. Indeed, different transverse modes at the input may excite the same resonance, i.e., a mode-independent resonance. As an example, in the resonators of Fig. 20c–d the transmission spectrum (third column) is the same for the two incident transverse modes (1 and 2). The mode-independent behavior of cascaded-mode resonators is a unique transmission characteristic, a feature verified experimentally in Fig. 22. This contrasts with traditional resonators, where different transverse modes exhibit different transmission spectra. Based on this property, it becomes possible to manipulate modes with different spatial profiles in an identical way using only one resonator.

5. 2 Experiments

We experimentally realize the proposed cascaded-mode resonators using the silicon-on-insulator (SOI) platform at telecom wavelengths (1550 nm). In our on-chip implementation, the cascaded modes have distinct transverse profiles TE_i, an in-plane polarization, and propagate along waveguides rather than in free space. The SOI

platform offers design flexibility in engineering the properties of the mode converters (reflection phase and magnitude), as well as the propagation properties of all modes participating in the cascade, such as their effective indices $n_{\mathrm{eff},i}$.

The device geometry is shown in Fig. 22 a,b together with scanning electron microscope (SEM) pictures of the fabricated structures. Materials. In general, each device consists of three main optical components: in- put/output waveguides that couple and guide light of chosen transverse modes to and away from the mode-converting resonators; a multi-mode waveguide section of length L_{wg} in which the cascaded modes are confined; specialized corrugated Bragg reflectors located on either side of the multi-mode waveguide that reflect one transverse mode into another. While, as described theoretically above, the number of conversions in a cascaded mode is only limited by the number of available transverse modes, we restrict our experimental demonstration to cascaded-mode resonators of the type shown in Fig. 20 that couple the two distinct transverse modes TE_0 and TE_2.

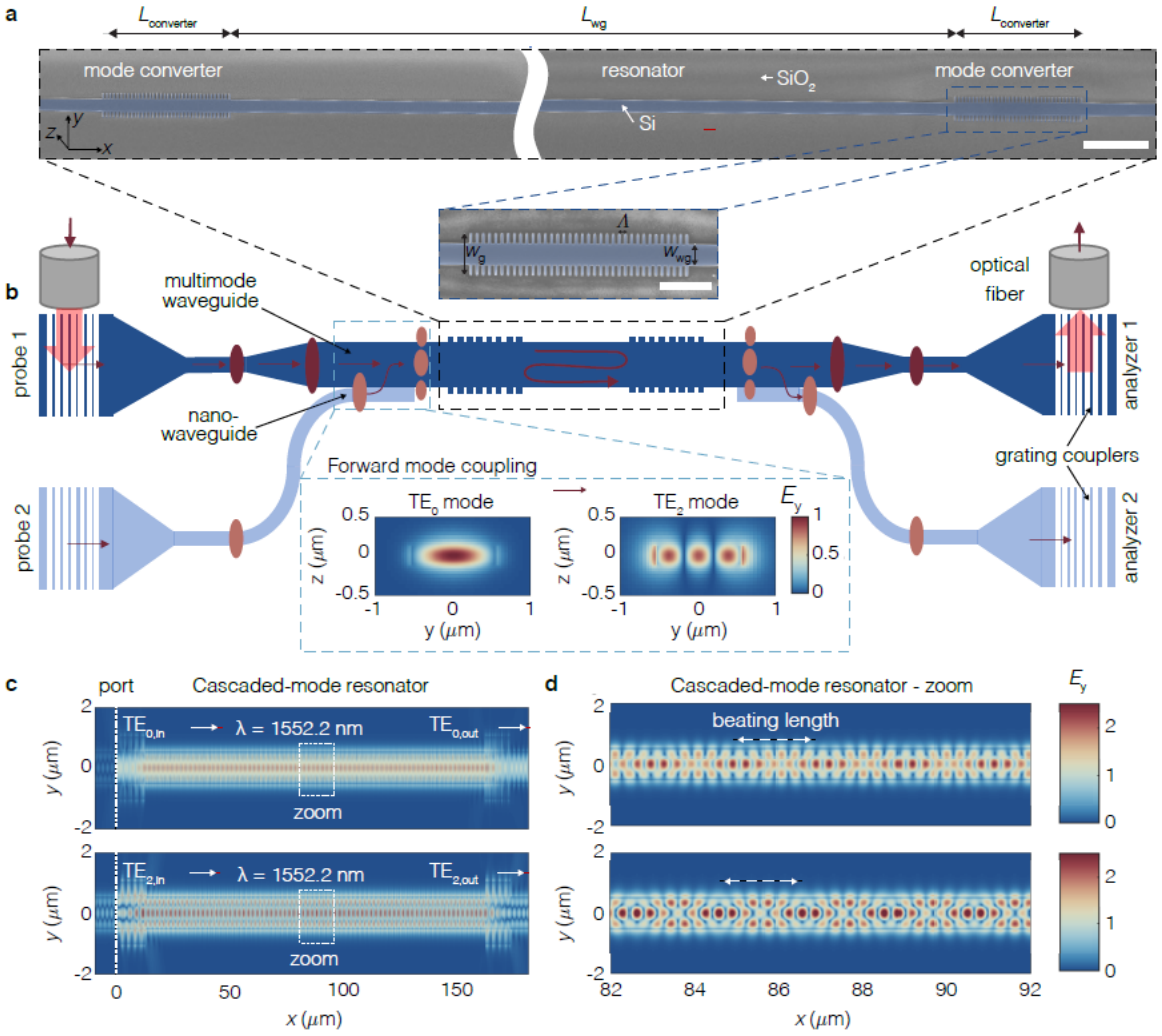

Fig. 22 | Experimental realization of cascaded-mode resonators in integrated photonics. a SEM pictures of the cascaded-mode resonator show two-mode converters connected via a multimode waveguide of width w_{wg} and length L_{wg}. Multimode waveguides located before and after the resonator guide telecom light into and outside the resonator. The mode converters are realized by corrugating the silicon waveguide laterally into the shape of a rectangular grating of periodicity Λ and width w_g. Scalebar = 5 μm and 2μm (inset). The periodicity Λ is chosen such that the phase-matching condition is satisfied for contra-directional coupling. The entire photonic circuit ridge is buried into a silica

layer. b Schematic of the device shows three different sections: 1. two input waveguides (left) that allow to probe the resonator with either TE0 (upper) or TE2 (lower), 2. the resonator region consisting of the multimode waveguide enclosed by the two mode converters, and 3. two analyzer waveguides which transmit the output of the resonator into two spatially separated locations, depending on its transverse profile TE_0 (upper) or TE_2 (lower). Probe 1 excites the TE_0 mode in the top waveguide. Probe 2 excites the TE_0 in the lower waveguide. This mode is converted into the TE_2 mode in the top multimode waveguide prior to the resonator via the forward-mode coupler, which operates on the principle that the effective index of the TE_0 mode in the nano-waveguide corresponds to the effective index of the TE_2 mode in the multimode waveguide. Similarly, analyzer 1 and analyzer 2 measure TE_0 and $_{TE2}$ modes, respectively. Spatially, the coupling occurs at the location where the nanowaveguide is in the immediate vicinity of the multimode waveguide. c Full-wave simulations of the telecom fields inside the cascaded-mode resonator demonstrate that self-consistent solutions of the round-trip condition occur at the same input wavelength for two distinct transverse modes $_{TE0}$ (upper) and TE_2 (lower). d Zoom into marked white region inside the resonator reveals the hybrid nature of the cascaded modes that arise as a superposition of counter propagating TE_0 or TE_2 modes with a characteristic beating length that does not depend on the input probe field.

Their transverse mode profiles are shown in the inset of Fig. 22 b. Consequently, the width of the waveguide in the cavity region (w_{wg} = 1.07 μm) was chosen such that it cuts off all transverse modes of a higher order than TE_2. In addition, the grating period Λ of the mode converters is chosen as to satisfy the phase-matching condition and provide the necessary momentum for the mode conversion to occur on the reflected wave: $2\pi/\Lambda = \Delta\beta_{12} = \beta_1 + \beta_2$, with $\beta_1 = \beta_{TE0} = n_{eff,TE0}\,\omega_0/c$ and $\beta_2 = \beta_{TE2} = n_{eff,TE2}\,\omega_0/c$ the propagation constants of the two coupled modes. This type of coupling is typically referred to as contra-directional coupling.

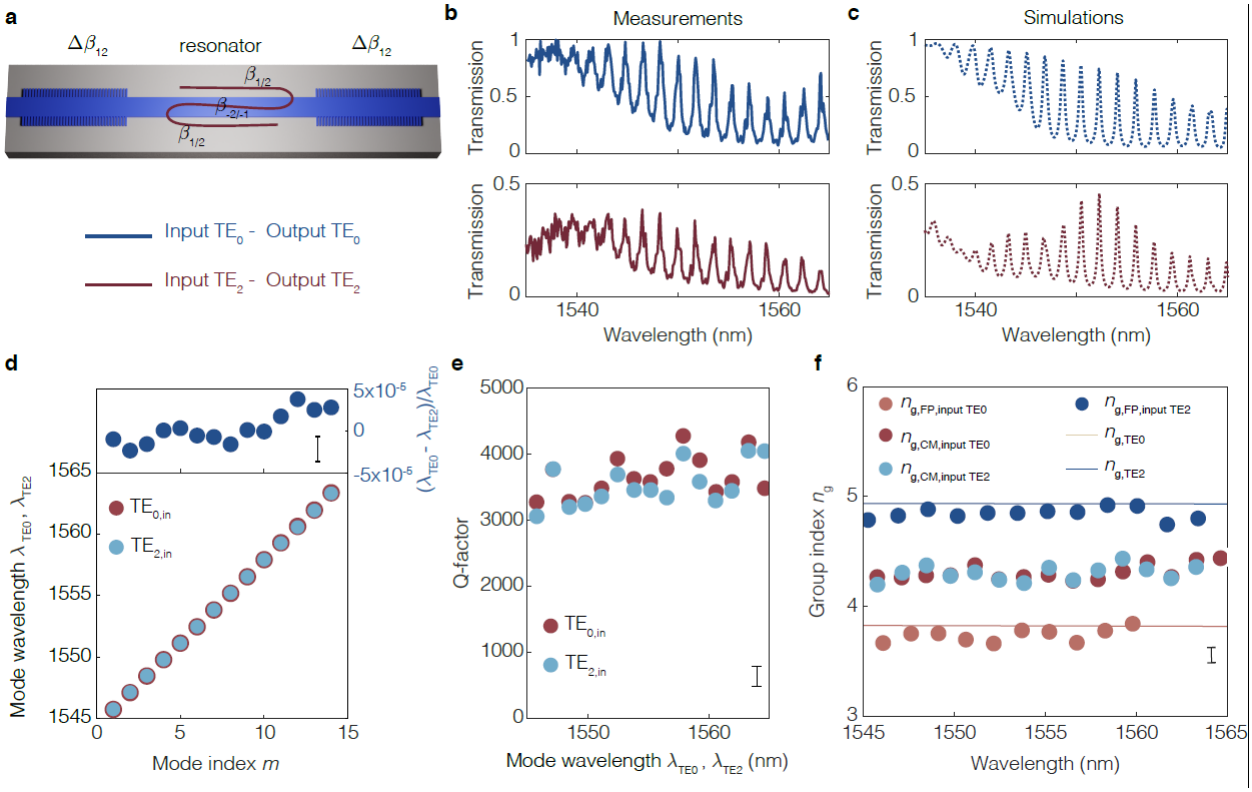

Fig. 23 Transmission spectroscopy of cascaded-mode resonators. a A cascadedmode resonator, where a reflection at both the left and the right Bragg mirror results into a conversion of the transverse mode from TE_0 to TE_2 and vice-versa. b The measured transmission spectra of the cascaded-mode resonator exhibit resonances regardless of whether TE_0 or TE_2 is

incident onto the resonator. c Simulated transmission spectra reproduce well the measurements. More measurement and simulation results are provided in the Supplementary Material. d–f Characteristic parameters of the cascaded-mode resonator extracted from the experimental transmission spectra. d The mode-independent character of cascaded-mode resonators is demonstrated by the fact that the resonant wavelengths of the cavity modes coincide in frequency (and wavelength), regardless of whether the resonator is probed by a TE_0 or TE_2 mode. The relative experimental mismatch between their resonant wavelengths is below $4 \times 10{-}5$, for all 13 considered modes, which is comparable to the experimental noise (upper panel). e Also the quality factors of the cascaded-mode resonator are mode-independent, as they coincide within the experimental error, regardless of whether the cascaded modes are excited by TE_0 or TE_2 inputs. The experimental error is calculated from the error of the fit of the resonance peaks. f In cascaded-mode resonators, the propagation constants change magnitude at each reflection off a mode-converting Bragg mirror, and the group indices of cascaded-mode (CM) resonances are equal to the arithmetic mean of conventional Fabry-Perot (FP) resonances in the same multimode waveguide. This property is confirmed experimentally, with TE_0 modes having a group index of 3.75, TE_2 modes having a group index of 4.85 and cascaded modes having a group index of 4.3. Full lines represent calculated group.

We now demonstrate in experiments and simulations the most evident signatures of cascaded-mode resonators: the mode-independent spectrum with modified spectral parameters. The symmetric cascaded-mode resonator of Fig. 20c provides resonant confinement to input modes that correspond to either TE_0 or TE_2 transverse modes and has the same transmission spectrum for either input. We confirm this computationally in Fig. 22c, where we report the simulated field profile of the same cascaded-mode resonator for the two possible inputs and find a locally enhanced field inside the resonator in both cases. Moreover, the hybrid nature of the near-infrared cascaded mode inside the resonator becomes apparent in the zoom-in of the spatial profile shown in Fig. 22d. The field profile can be decomposed into a superposition of counter propagating TE_0 and TE_2 waveguide modes that exhibit, as expected, the same beating length for both inputs (marked by the white arrow). We demonstrate this property experimentally by transmission spectroscopy and contrast it with two test Fabry-Perot resonators that employ standard mirrors and provide cavity confinement to only one of TE_0 or TE_2 modes. The experimental results are shown for the three cases in Fig. 23 a-c. We find that cavity modes appear, as expected, for both TE_0 and TE_2 modes in the case of the cascaded-mode resonator only. Moreover, the experimental results are well-reproduced by our simulations. Cavity modes appear only for one of the two modes for the conventional Fabry-Perot resonators, while light is simply transmitted for the other modes.

Next, we analyze the resonator properties of the cavity modes associated with the cascaded-mode resonators compared to the conventional Fabry-Perot modes in Fig. 23d-fFirstly, we show in Fig. 23d that the intra-cavity modes of the cascaded-mode resonators excited by the two inputs (TE_0 or TE_2) coincide in frequency. We experimentally find a negligible relative deviation between the two sets of resonant wavelengths of $\approx 4\text{x}10^{-5}$. Furthermore, the quality factors of the two sets are approximately equal, as shown in Fig. 23e. Finally, the group index of the cascaded modes is approximately equal to $n_g = 4.3$, regardless of whether they are excited by TE_0 or TE_2. In contrast, the group index of the Fabry-Perot modes are equal to $n_{g,TE0} = 3.75$ and $n_{g,TE2} = 4.85$ (Fig. 23f). This result confirms once more the cascaded-mode character of the measured spectra, particularly because the group index is approximately the arithmetic mean of the group indices of the participating transverse modes.

5.3 Prospects for non-reciprocal devices

The cascaded-mode resonator has a broken mirror-symmetry, which lays the foundation for broken reciprocity.

However, the mechanism is a bit more subtle; it is known that reciprocity can only be broken in one of the following 3 ways: by including materials with magneto-optic interactions, nonlinear interactions, or explicit time-dependent material parameters. Now, a nonlinear material in itself is not enough to break the reciprocity of a system (e.g. about a traditional nonlinear cavity). The crux of the story now is that the cascaded-mode resonator can be made non-reciprocal by including a nonlinear material inside the cavity because the nonlinear material can be tailored to only be phase matched with the mode propagating in one the two directions. This would create broken reciprocity behavior.

Papers

M.L. Meretska, F. H. B. Somhorst, M. Ossiander, Y. Hou, J. Moodera, and F. Capasso "Measurements of the magneto-optical properties of thin-film EuS at room temperature in the visible spectrum." *Applied Physics Letters* **120**, 25 (2022). Data made available to the public https://refractiveindex.info/?shelf=main&book=EuS&page=Meretska.

F. H. B. Somhorst, M.L. Meretska, M. Ossiander, Y. Hou, J. Moodera, and F. Capass**o** " Magneto-optical properties of e-beam evaporated EuS films for room temperature applications" *Proceedings of the European Conference on Integrated Optics (ECIO)* 2023 https://www.ecio-conference.org/2023-proceedings/

Vincent Ginis, Ileana-Cristina Benea-Chelmus, Jinsheng Lu, Marco Piccardo, and Federico Capasso "Resonators with tailored optical path by cascaded-mode conversions." *Nature Communications* **14,** 495 (2023)

Honors – Federico Capasso

2023 Selected as Citation Laureate, one of 23 worldwide in science, by the Institute for Scientific Information (ISI)™ at Clarivate; "for pioneering research on photonics, plasmonics, and metasurfaces, as well as contributions to the invention of and improvements on the quantum cascade laser." https://clarivate.com/news/clarivate-unveils-citation-laureates-2023-annual-list-of-researchers-of-nobel-class/

2021 Ives Medal and Jarus Quinn Prize of Optica "for seminal and wide-ranging contributions to optical physics, quantum electronics and nanophotonics" The highest award of Optica (formerly OSA)

26th Micro-optics Conference Award "for pioneering contributions to quantum cascade lasers, plasmonic and metamaterials" Hamamatsu City, Japan

Participants

- Graduate students: Zhongpeng Sun
- Undergraduate students: F. H. B. Somhorst.
  Received a Master degree at Twente University based on the magneto optic work here reported
- Postdocs: Maryna Meretska, Christina Benea Chelmus, Marcus Ossiander, Jinsheng Lu

Collaborators

- Prof. Jagadeesh Moodera (MIT), Y. Hou (MIT)
- Prof. Vincent Ginis, Free University of Brussels and Harvard University

- Marco Piccardo, Italian Institute of Technology